J. Fluid Mech. (2005), *vol.* 535, *pp.* 255–285. © 2005 Cambridge University Press
doi:10.1017/S0022112005004830 Printed in the United Kingdom

Dissolution-driven convection in a reactive porous medium

By MARK A. HALLWORTH[1], HERBERT E. HUPPERT[1] AND ANDREW W. WOODS[2]

[1]Institute of Theoretical Geophysics, Department of Applied Mathematics and Theoretical Physics, Centre for Mathematical Sciences, University of Cambridge, Wilberforce Road, Cambridge CB3 0WA, UK

[2]BP Institute, Madingley Rise, University of Cambridge, Madingley Road, Cambridge CB3 0EZ, UK
hallworth@esc.cam.ac.uk; heh1@esc.cam.ac.uk; andy@bpi.cam.ac.uk

(Received 27 February 2004 and in revised form 5 February 2005)

The heating from above of an initially homogeneous layer of solid crystals, saturated liquid and glass ballotini (an inert matrix filler) is considered both experimentally and theoretically. The heat flux causes crystals at the top of the layer to dissolve, forming liquid which, being more concentrated and dense than the interstitial liquid below, drives convection in the lower layer. Mixing of this high-concentration liquid into the lower layer leads to precipitation, thereby releasing latent heat which raises the temperature of the lower layer. Dissolution of solid crystals from the top leaves behind a closely packed layer of glass ballotini overlain by a layer of clear liquid, both of which deepen with time. The initially homogeneous porous medium thus develops into a three-layer stratified system of (from the top): clear liquid; clear liquid with close-packed ballotini; and the evolved initial assemblage of solid crystals, ballotini and saturated liquid. Data from laboratory experiments compare well with analytical and numerical results from a one-dimensional theoretical model. The model is based on the concept that the heat supplied from above is used entirely for the dissolution of solid crystals at the upper boundary of the lower layer. The resulting compositional convection redistributes the dissolved salt uniformly throughout the lower layer, where it partly recrystallizes to restore chemical equilibrium. The crystallization and associated release of latent heat leads to a gradual and uniform increase of both the solid fraction and temperature of the lower layer. Some geological consequences of the model are presented in the concluding section.

1. Introduction

Fluid dynamical processes in porous media play an important role in a wide range of industrial and natural situations. These include the recovery of oil, the percolation of water through soils, the geological formation of mineral deposits and the crystallization of molten rocks. A description of some of the fundamental processes is given in Bear (1979) and Phillips (1991). Some of these processes involve reactions which cause precipitation, dissolution or melting of various phases within the medium, subjects reviewed by Huppert (1990), Phillips (1991) and Worster (2000). An important consequence of such phase changes is that the volume fraction of the solid matrix changes with time. In this paper we commence a series of experimental and related theoretical investigations of how a porous medium comprising both individual crystals

https://doi.org/10.1017/S0022112005004830 Published online by Cambridge University Press

and saturated liquid reacts to an imposed temperature field. The evolution of the porosity and the transfer of heat and mass is followed in detail.

One of the motivations for this work is its application to the geological fluid mechanics of evolving magma chambers, which are reservoirs of molten or partially molten rock (magma) within the Earth's crust. The rocks which solidify from large intrusions of basaltic magma frequently exhibit textures which suggest they formed as an accumulation of dense crystals settling on the chamber floor (Wager, Brown & Wadsworth 1960). These so-called *cumulates* invariably display horizontal layering, as defined by vertical changes in the modal proportions of their constituent minerals (Wager & Brown 1968; Irvine 1982). In general, accumulations of settled crystals initially incorporate a comparable volume of liquid occupying the interstices between grains. This liquid must eventually solidify, but it may not do so *in situ*, since both compaction and convective processes will cause liquid to move relative to the solid framework. Post-cumulus melt migration is now recognized as a fundamental process in the compositional modification of cumulates as they evolve from porous media to their final solid state (Irvine 1987; Sparks *et al.* 1985; Hallworth 1998).

Previous research aimed at investigating the fluid dynamics of migrating interstitial melt has concentrated on convective motion arising through the cooling and crystallization of interstitial liquid (Kerr & Tait 1986). Our interest in this paper focuses on the consequences of introducing new interstitial liquid which is not in equilibrium with the surrounding solid matrix, and is capable of melting or dissolving some or all of its components. Two situations could be considered. The first is the straightforward heating of a porous medium caused by contact against a hot, intrusive body. The second is more complicated, and involves the displacement of original equilibrium melt by the input of new, higher temperature melt of more primitive chemical composition (Jupp & Woods 2003). In either case, the original solid matrix becomes immersed in a liquid into which it may partially dissolve. This scenario is particularly relevant to *open system* magma chambers, that is those which are periodically replenished by new magma from deeper source regions.

We are concerned with the fluid dynamical effects of matrix dissolution and, in particular, how density changes to the evolving liquid modify the transfer of mass and heat. We also examine how the matrix structure evolves due to dissolution or precipitation. To investigate these ideas, we performed a series of laboratory experiments in which a porous medium, consisting of a mixture of loosely packed solid crystals bathed in saturated interstitial liquid, was heated from above. The assemblage was initially in both thermal and chemical equilibrium. Upon heating, the increase in temperature of the interstitial liquid at the top of the layer caused some fraction of the enveloped solid matrix to dissolve. In the situation described here, dissolution of the solid matrix into interstitial liquid leads to an overall increase in the local liquid density, causing compositionally driven convection. One of the primary aims of the investigation was to determine how this compositional convection affects the thermal and chemical evolution of the system.

The chemical system we used in the experiments was the binary KNO_3–H_2O system. The relevant portion of the phase diagram for this system is displayed in figure 1, and shows part of the super-eutectic liquidus curve. The solubility of KNO_3 in water is strongly temperature dependent (the liquidus gradient for KNO_3 is much less steep than for most other common aqueous salt systems), and results in large changes in the concentration of saturated solutions for relatively small changes in temperature. This feature amplifies the amount of dissolution or precipitation over the temperature range that is feasible in the laboratory.

https://doi.org/10.1017/S0022112005004830 Published online by Cambridge University Press

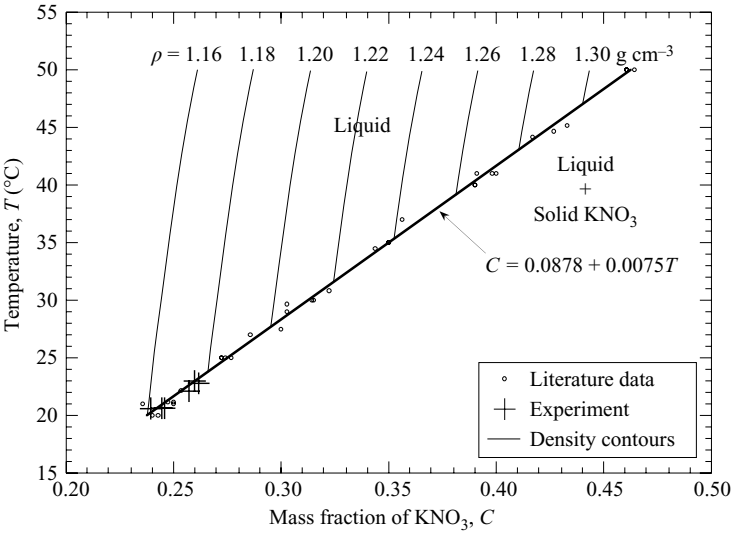


FIGURE 1. Part of the phase diagram for KNO_3, with the best-fit linear C–T relationship to the data, symbolized by o, given by (3.1) for the (super-eutectic) liquidus between 20 °C and 50 °C, including selected density contours in the liquid region (data from Washburn 1962). The initial temperature and concentration of interstitial fluid in the various experiments are indicated by crosses.

Our results indicate that heating an initially homogeneous, reactive porous medium from above causes extensive redistribution of material and can generate horizontal layers of markedly different composition. The conductive transfer of heat is buffered at a descending interface, where it supplies the heat necessary for the dissolution of solid crystals into the interstitial liquid. The resulting increase in the density of this liquid drives compositional convection, which distributes the dissolved solid throughout the underlying porous layer. The subsequent recrystallization of dissolved solid and the associated release of latent heat then cause a uniform increase in both the solid fraction and temperature of the lower layer.

We describe the details of our experimental setup and the results which we observed both qualitatively and quantitatively in the next section. A theoretical model is presented in § 3 and the quantitative predictions compared with the experimental data. We describe further applications of our new concepts in the final section.

2. Experiments

2.1. *Apparatus*

The experiments were conducted in a Perspex tank with internal horizontal dimensions of 2 cm by 30 cm, and a depth of 43 cm, as depicted in figure 2. The narrow 'cell' design was chosen so that backlit illumination would penetrate the porous medium and thus allow two-dimensional visualization of the fluid dynamics. The tank was constructed from two vertical parallel plates of 11 mm thick Perspex separated by three 2 cm wide Perspex spacer blocks forming the remaining two sidewalls and base (figure 2*a*). These components were bolted together using external clamp bars to distribute the load, and were sealed using O-rings inset around the perimeter of the spacer blocks. This assembly allowed the tank to be dismantled after each experiment for the purpose of sampling the residual solid matrix. A nozzle was fitted to the base of the tank to

https://doi.org/10.1017/S0022112005004830 Published online by Cambridge University Press

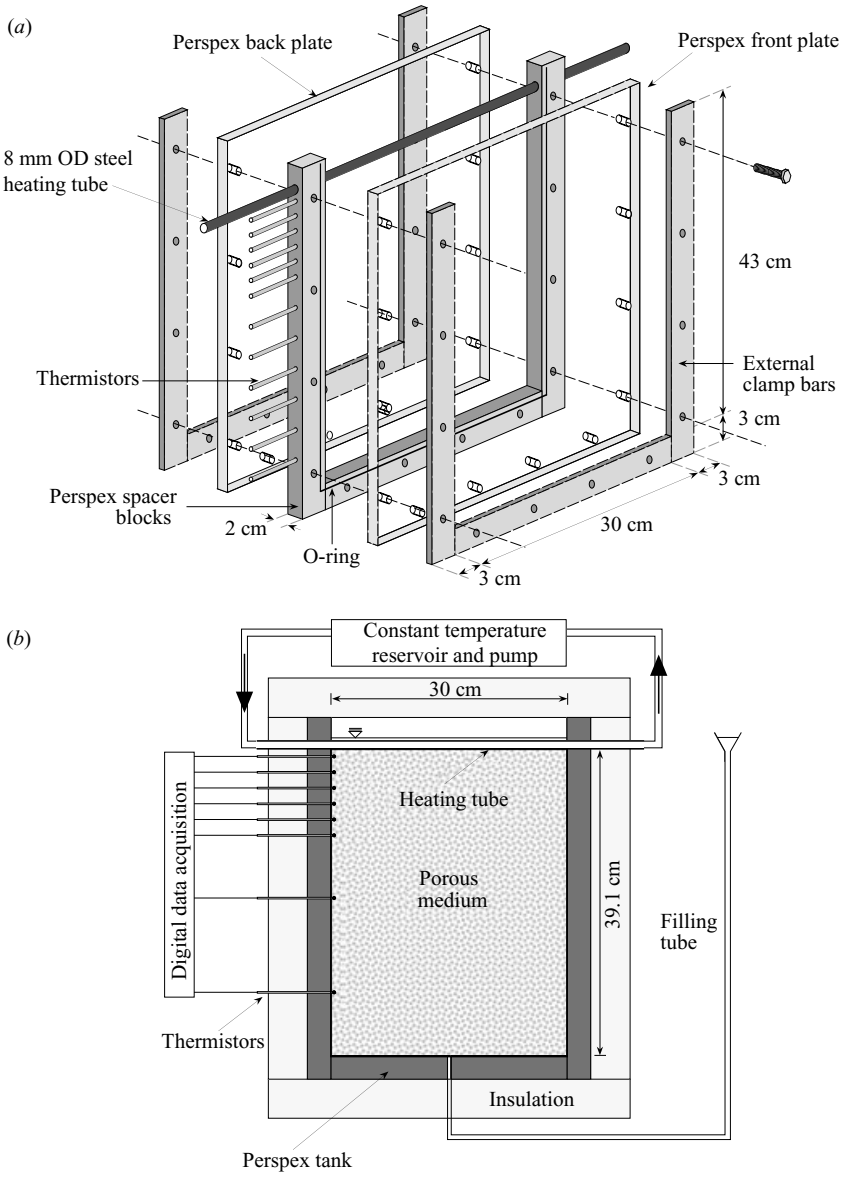


FIGURE 2. The experimental apparatus. (*a*) An exploded view showing the tank construction. (*b*) A schematic of the experimental system.

allow filling and drainage of interstitial liquid, and holes spaced every 2 cm between heights of 2 cm and 38 cm from the base up the centre of one sidewall spacer block permitted the insertion of an array of thermistor probes at selected positions. Heating at the top of the porous medium was supplied by a steel tube of external diameter 8 mm which passed horizontally through both sidewall spacer blocks, centred at a height of 39.5 cm from the base. Heated water was pumped through this tube at a rate of 15 l min^{-1} in a continuous loop from a temperature-controlled reservoir of 12 l capacity, which was maintained throughout all the experiments at $50.0 \pm 0.1\,^{\circ}$C. Heat loss to the laboratory was reduced by insulating the tank on all sides with 5 cm thick

https://doi.org/10.1017/S0022112005004830 Published online by Cambridge University Press

	Solid matrix		Interstitial liquid			Bulk system						
Expt no.	m_g (g)	m_s (g)	m_l (g)	C_o	ρ_l (g cm^{-3})	Glass ϕ_g	KNO_3 ϕ_s	Liquid ϕ_l	Solid ϕ_o	T_o (°C)	$\overline{C_0}$	M_s (g)
100% ballotini matrix												
1	3517	–	989	0.00	0.9982	0.582	–	0.418	0.582	19.3	0.00	–
100% KNO_3 matrix												
2a	–	2152	1630	0.245	1.1661	–	0.437	0.563	0.437	22.6	0.675	2551
2b	–	2187	1659	0.262	1.1791	–	0.441	0.559	0.441	22.8	0.682	2622
50% ballotini/50% KNO_3 matrix												
3a	1875	1338	1216	0.257	1.1750	0.306	0.264	0.430	0.570	22.2	0.646	1650
3b	1886	1398	1247	0.256	1.1738	0.300	0.269	0.431	0.569	22.8	0.649	1717
3c	1753	1362	1276	0.246	1.1669	0.293	0.275	0.432	0.568	21.9	0.635	1676
75% ballotini/25% KNO_3 matrix												
4	2694	735	1224	0.239	1.1615	0.450	0.148	0.401	0.599	20.2	0.528	1034

TABLE 1. Initial conditions of the various porous media heated from above. The column headings are defined in the text with the exception of $\overline{C_o}$, the bulk concentration of KNO_3, and M_s, its total mass, both of which remain constant throughout the experiment.

expanded polystyrene and lagging the pipework connecting the heating tube to the reservoir.

2.2. *Procedure*

The experimental procedure began by preparing the porous medium, which was composed of a matrix-supported mixture of solid crystals of KNO_3 and varying proportions of 3 mm diameter glass ballotini, bathed in an interstitial liquid of aqueous KNO_3 solution saturated at room temperature. The solid KNO_3 crystals were specially grown from supersaturated solutions of the commercially available powder in large crystallization tanks, before being dried and seived to yield a harvest of well-formed, tabular to bladed crystals varying in size from 2 to 10 mm. For experiments in which the solid matrix was composed entirely of KNO_3, the tank was filled with a measured mass m_s of dry crystals up to the base of the heating tube at a height H of 39.1 cm. In other experiments, solid KNO_3 crystals were uniformly mixed with a mass m_g of glass ballotini. The glass in these cases simply acted as an inert matrix filler, and allowed us to vary the total mass of KNO_3 available for dissolution while still maintaining a self-supporting matrix up to the required height. To ensure a homogeneous initial distribution of the two solid phases, the tank was filled in mm-scale height steps by successive additions of small ($\approx 10\,\mathrm{cm}^3$) volumes of the correctly proportioned mixture. Once the solid matrix was *in situ* and the heating tube had been positioned to just touch its upper surface, the porous pile was then immersed in a mass m_l of a saturated solution of KNO_3 of initial concentration C_o at (room) temperature T_o. The liquid was fed slowly into the tank at its base to eliminate any trapped pockets of air, and was filled beyond the top of the solid matrix to a height of 40.3 cm so that it completely submerged the heating tube, thus ensuring good thermal contact. The initial conditions of all solid and liquid components of the porous medium are presented in table 1. Values of the initial volume fraction ϕ of solid KNO_3, glass and interstitial liquid (denoted by subscripts s, g and l respectively),

https://doi.org/10.1017/S0022112005004830 Published online by Cambridge University Press

	Water @ 32 °C	25wt.% KNO_3 soln.@ 32 °C	Glass ballotini	Solid KNO_3	Perspex
ρ (g cm^{-3})	0.9950	1.1636	2.55	2.109	1.20
c_p (cal g^{-1} °C^{-1})	0.9980	0.9940	0.27	0.22	0.36
κ (cm^2 s^{-1})	1.4×10^{-3}	1.1×10^{-3}	2.9×10^{-3}	–	0.9×10^{-3}
L (cal g^{-1})	–	–	–	84	–

TABLE 2. Values of physical properties and thermochemical data of the various solid and liquid phases. (Data from Washburn 1962; Weast 1971).

were calculated using

$$\phi_s = \frac{m_s}{\rho_s A H}, \quad \phi_g = \frac{m_g}{\rho_g A H}, \quad \phi_l = 1 - (\phi_s + \phi_g), \tag{1.1a, b, c}$$

where ρ_s and ρ_g are the densities of solid KNO_3 and glass respectively (as given in table 2), and $A = 60\,\text{cm}^2$ is the horizontal cross-sectional area of the tank. The initial total solid volume fraction ϕ_o is simply the sum of ϕ_s and ϕ_g. We draw attention to the fact that the value of $\phi_o \approx 0.44$ for the pure KNO_3 cases is substantially lower than that for KNO_3/glass mixtures ($\phi_o \approx 0.59$), and reflects the more efficient packing ability of spheres over randomly orientated, bladed crystals.

The experiments were started by circulating water at a temperature of 50 °C through the heating tube. As the heating progressed, dissolution of the solid matrix occurred, and was monitored by recording the heights of the top of the matrix and any internal interfaces as a function of time to within 1 mm. This was done by tracing their profiles on to translucent, gridded paper fixed to the front plate. The thermal evolution of the system, with an accuracy of 0.1 °C was continually monitored by digital acquisition of data from an array of 8 thermistors positioned at various fixed heights down one sidewall of the tank. The thermistor beads themselves only extended ≈ 2 mm into the porous medium, since further horizontal penetration of the probes might have hindered any downward compaction of the matrix as a result of solid dissolution. A check on how representative these sidewall temperature measurements are is discussed in the next section.

A total of seven experiments was performed, as indicated in table 1. The experiments were generally left to run for 24 hours, but heat loss to the laboratory became a significant factor after roughly 10 hours. This was unfortunate, because the system had not reached thermal equilibrium, as seen clearly in the experimental results. Moreover, the theoretical model presented in § 3 indicates that equilibration takes a time of order tens of days, well beyond the time we could adequately insulate the system in our laboratory. At the end of each run, the concentration of the interstitial liquid at various heights was determined by measuring the refractive index of withdrawn samples using a hand-held refractometer. Sample withdrawal was not performed during the course of any run since the significant loss of fluid volume from the system would have displaced the thermal profile as well as causing loss of contact of fluid with the heating tube. Once drained of interstitial fluid, the tank was laid horizontally and the front panel removed to gain access to the residual solid matrix, which was then sectioned into 2 cm wide sample strips across the width of the tank. Each sample was dissolved in a known mass of water and its refractive index measured to determine the amount of KNO_3. If glass ballotini were present, their mass was recovered by drying and weighing. In this manner, the proportions

https://doi.org/10.1017/S0022112005004830 Published online by Cambridge University Press

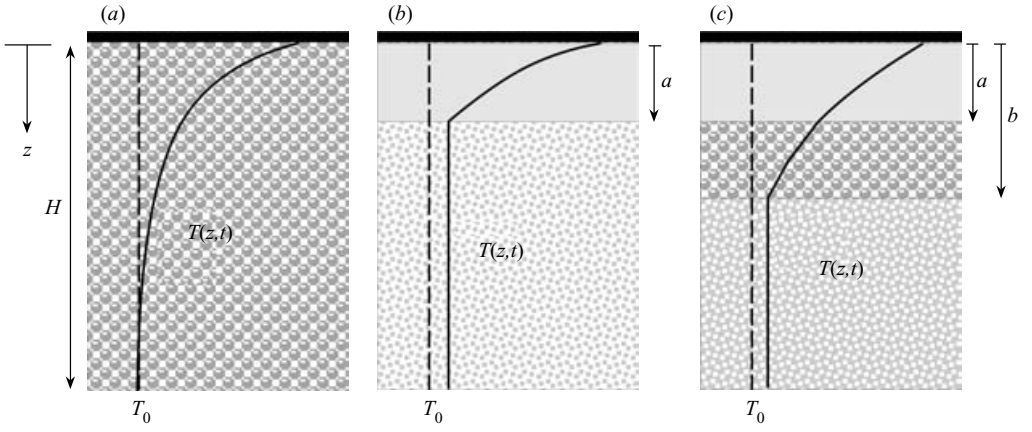


FIGURE 3. Schematic representations of the three experimental variations, including the temperature profile developed in each case. (*a*) Ballotini in water, (*b*) KNO_3 in solution, (*c*) KNO_3 + ballotini in solution.

and amounts of residual solid matrix per unit volume as a function of height were determined.

2.3. *Results*

2.3.1. *Ballotini in water*

In order to test the thermal behaviour of the experimental tank and heating system, a preliminary experiment (1) was conducted using a porous bed composed entirely of 3 mm glass ballotini immersed in pure water (figure 3*a*). In this situation, the solid matrix and interstitial fluid are completely unreactive, and there is no possibility of solutal convection. Heating from above should thus result in the development of a stable thermal gradient which evolves in response to conductive heat transfer through the composite porous medium.

The temperature measurements from an array of eight thermistors fixed at 4 cm intervals between heights of 8 cm and 36 cm from the base are presented as functions of height h at selected times t in figure 4*a*. The data show typical conductive profiles, which may be compared to the standard similarity solution for a conductive temperature profile in a semi-infinite medium (Carlsaw & Jaeger 1959), expressed for the present situation as

$$T = T_B + (T_W - T_B)\mathrm{erfc}(\eta) \tag{2.1}$$

with

$$\eta = \frac{a}{2\sqrt{\bar{\kappa}t}}, \tag{2.2}$$

where T is the temperature at a distance a $(= H - h)$ from the heating tube at time t, T_W and T_B are the temperatures of the heating tube and base of the tank respectively, and $\bar{\kappa}$ is the effective thermal diffusivity of the system. Since the thickness of the Perspex walls of the container $d = 1.1$ cm is comparable to the half-width of the tank $w = 1.0$ cm, heat conduction down the walls must be accounted for, and the appropriate value of $\bar{\kappa}$ is the correctly weighted sum of the values for glass, water and Perspex (given in table 2), as expressed by

$$\bar{\kappa} = \frac{w[\phi_o\kappa_g + (1-\phi_o)\kappa_w] + d\kappa_p}{w + d}, \tag{2.3}$$

https://doi.org/10.1017/S0022112005004830 Published online by Cambridge University Press

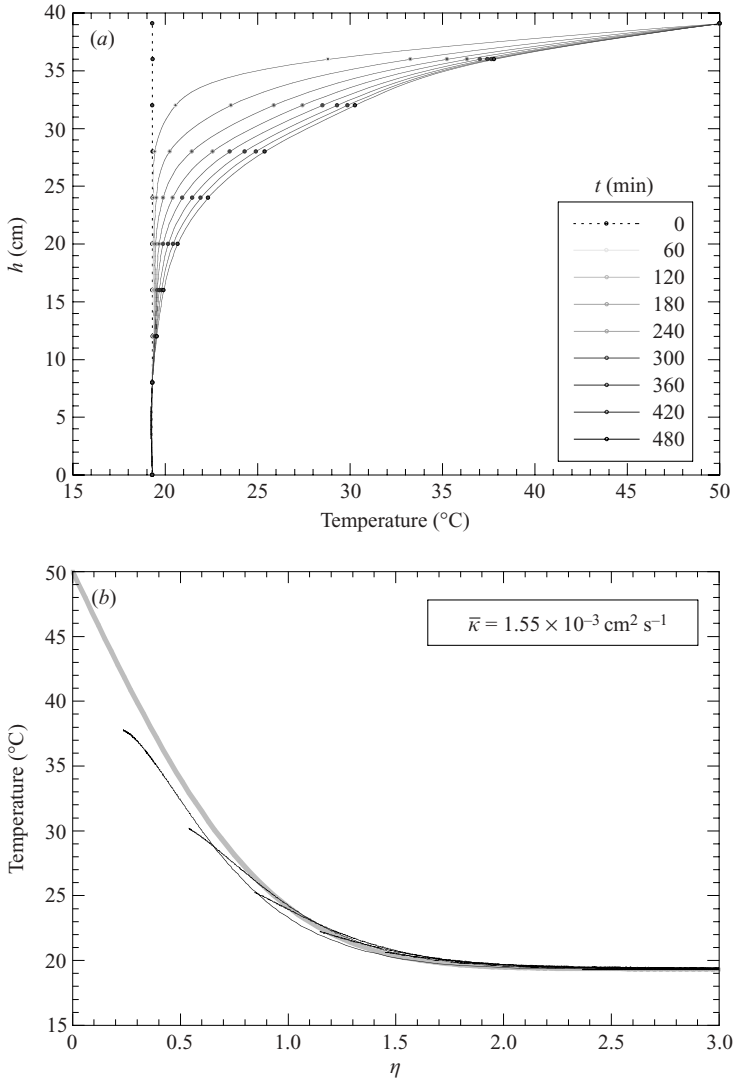


FIGURE 4. (*a*) Temperature measurements as a function of height at selected times in Expt 1, showing the typical conductive profile developed when a porous bed of glass ballotini immersed in water is heated from above. (*b*) Temperature as a function of η for the scaled data compared with the theoretical curve given by (2.1).

where ϕ_o is the solid volume fraction of ballotini, with a measured value of 0.58. figure 4(*b*) plots T as a function of η for the scaled data compared to the theoretical curve given by (2.1). The data (incorporating a small correction to eliminate heat input from the laboratory) show a good collapse and close agreement with the theoretical curve. The result indicates that the thermal behaviour of the experimental tank responds in a predictable manner to the heating system, and lends a degree of confidence to subsequently described experiments. (We mention here that several earlier attempts at this experiment failed to yield good results due to a design flaw in the tank. The external clamp bars were originally made from metal, and caused anomalously high temperatures of fluid in the lower region of the tank as a result of heat conduction down their length. The problem was rectified by replacing the metal

https://doi.org/10.1017/S0022112005004830 Published online by Cambridge University Press

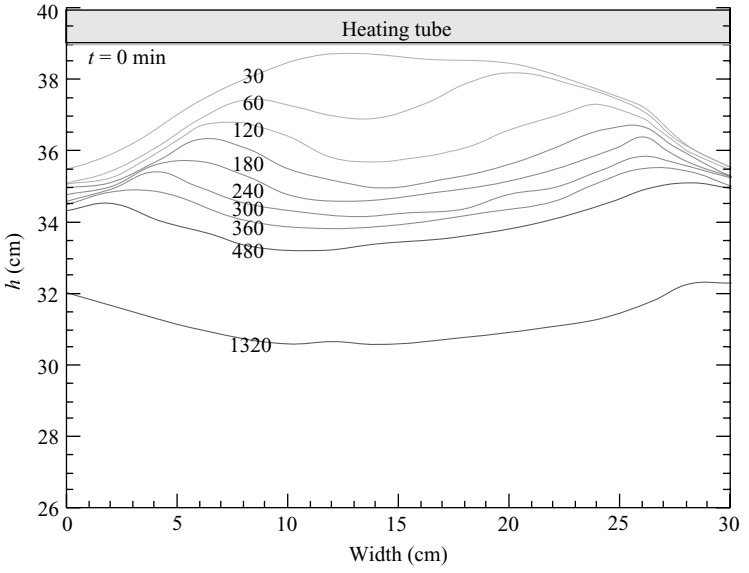


FIGURE 5. A plot showing the height of the interface across the width of the tank at selected times during Expt 2a.

bars with Perspex equivalents, but this emphasizes the care necessary in designing experimental equipment and justifies the effort expended in test experiments.)

2.3.2. *Solid KNO_3 in saturated KNO_3 solution*

Two (repeat) experiments (2a and 2b) were performed using a matrix-supported layer of loosely packed KNO_3 crystals, with $\phi_o \approx 0.44$, immersed in saturated KNO_3 solution, initially in compositional and thermal equilibrium at room temperature (table 1 and figure 3*b*). Upon heating, the interstitial liquid at the top of the layer immediately began to dissolve the enveloped solid crystals, increasing both its composition and density and becoming gravitationally unstable. This initiated the onset of compositional convection in the form of descending plumes of relatively warm, dense liquid with an equivalent upflow of cooler, saturated interstitial liquid replenishing the interfacial region. The convective plumes were visualized by dye streaks from small potassium permanganate crystals dropped on to the interface, and were observed to percolate through the entire porous medium, establishing a general convective circulation. As the KNO_3 crystals dissolved, a descending interface formed, defined by a plane separating the uppermost limit of a layer of solid crystals and an overlying layer of clear liquid. The dissolution of KNO_3 crystals appeared to occur primarily in a 1 to 2 mm thick zone directly beneath the descending interface. No discernible decrease in crystal grain size or evidence of compaction was observed below this thin zone of dissolution, which suggested that the decrease in height of the crystal matrix layer with time was due to corrosion at its top, rather than due to compaction in response to solid volume loss throughout its depth. However, the interface between the two layers was typically undulating, with localized regions of more intense dissolution forming transient interfacial depressions above the major sources of descending plumes, and correspondingly less dissolution and interface 'highs' in regions of interstitial liquid upwelling. Over time, however, the general convective circulation pattern would change and switch the regions of contrasting dissolution rate. This is illustrated in figure 5, which plots the interface height as a

https://doi.org/10.1017/S0022112005004830 Published online by Cambridge University Press

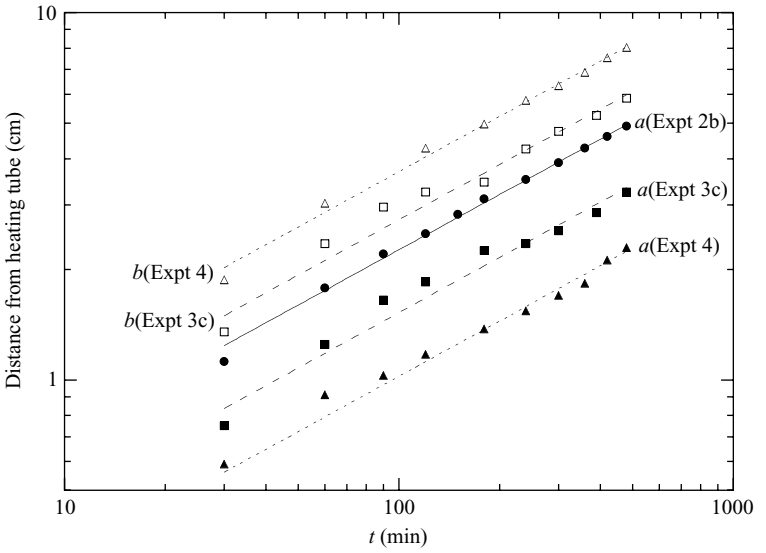


FIGURE 6. The mean height of the interfaces, measured in terms of the distance from the heating tube, plotted as a function of time for experiments with varying initial volume fractions of KNO_3 as described in table 1. The straight lines through the data points are the individual best-fit curves according to a relationship of $t^{1/2}$. Their constants of proportionality are given in table 3.

function of width across the tank at selected times for Expt 2a. The mean height of the interface, measured in terms of distance a from the heating tube, is plotted as a function of time on logarithmic axes in figure 6.

The descent of warm, dense plumes and the general thermal evolution of the system were monitored by an array of eight thermistors at fixed heights of 8, 20, 28, 30, 32, 34, 36 and 38 cm from the base. Temperature data from this array for Expt 2a are presented as functions of time and height in figure 7. In figure 7(a), the time axis is plotted on a logarithmic scale to illustrate the complex thermal structure that exists in the early phase of development. Temperature traces for roughly the first 50 minutes are characterized by periods of rapid heating events. We interpret these as corresponding to the passage of descending plumes of warm, high-concentration interstitial fluid from the interface as they encounter thermistors at different heights. As the plume locations switch positions, the thermistors revert to recording the mean temperature of the lower porous layer, which is seen to increase gradually but remain fairly uniform throughout its depth. At later times, the emergence of individual thermistors into the upper clear layer at sequential heights, and the thermal gradient there, is also readily apparent. Similar temperature plots from the other experiments involving dissolution of solid KNO_3 all exhibit essentially the same pattern of early, periodic overturn events and a gradual increase in the mean temperature of the lower layer. However, the exact timing of temperature 'spikes' differs from run to run, and is controlled by the somewhat random convective circulation pattern that is established in relation to the positioning of the thermistors along one sidewall of the tank. In figure 7(b), temperature measurements from Expt 2a are plotted as a function of height for selected times. These profiles illustrate the strong thermal gradient that develops in the upper clear layer, and the gradual increase in temperature of the lower layer, which remains essentially uniform throughout its depth.

https://doi.org/10.1017/S0022112005004830 Published online by Cambridge University Press

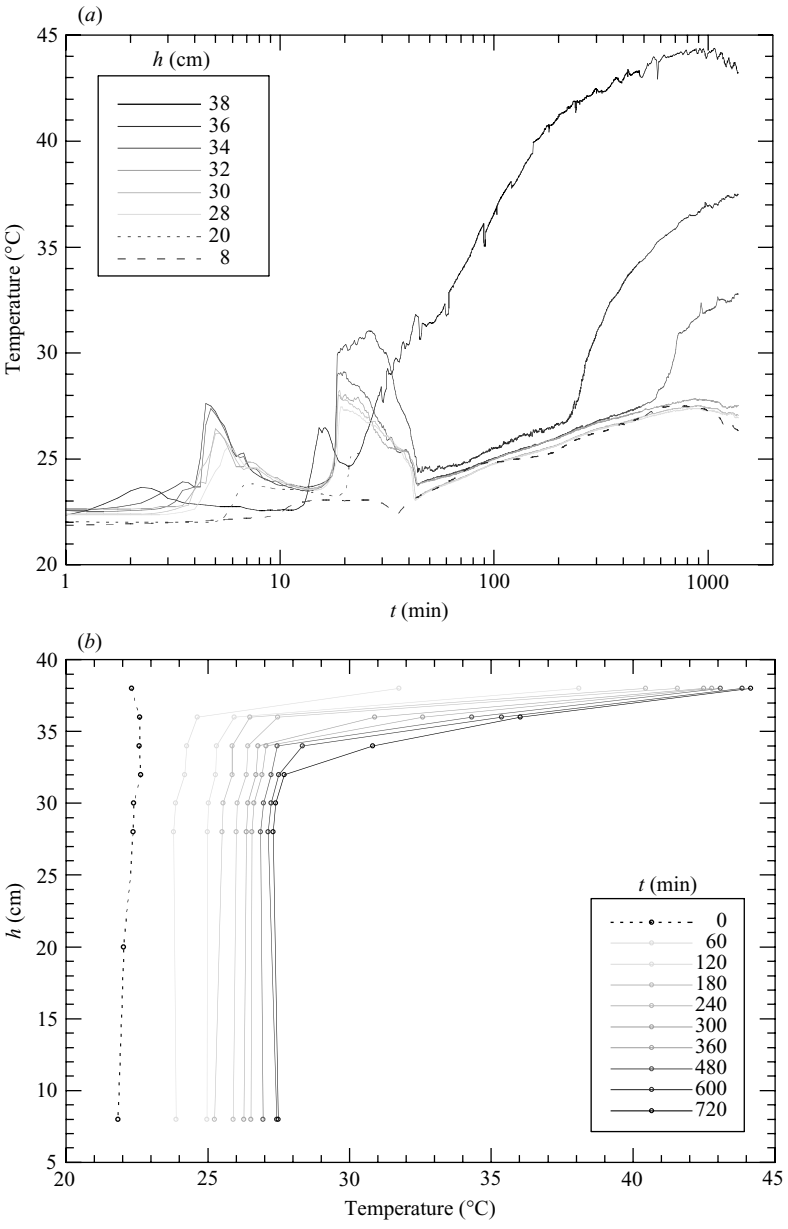


FIGURE 7. The temperature data from an array of eight thermistors at different heights in Expt 2a plotted against (*a*) time, and (*b*) height at selected times.

At the end of each experiment, the final assemblage was analysed to determine the relative volumetric proportions of solid and liquid as a function of height. The results of this analysis from Expt 2a are presented in figure 8(*a*). A clear increase in the solid fraction of KNO_3 in the residual solid matrix is observed when compared with the initial value of $\phi_o = 0.44$. This additional solid material has evidently crystallized from liquid that convected downwards from the overlying region of dissolution which is now devoid of crystals.

https://doi.org/10.1017/S0022112005004830 Published online by Cambridge University Press

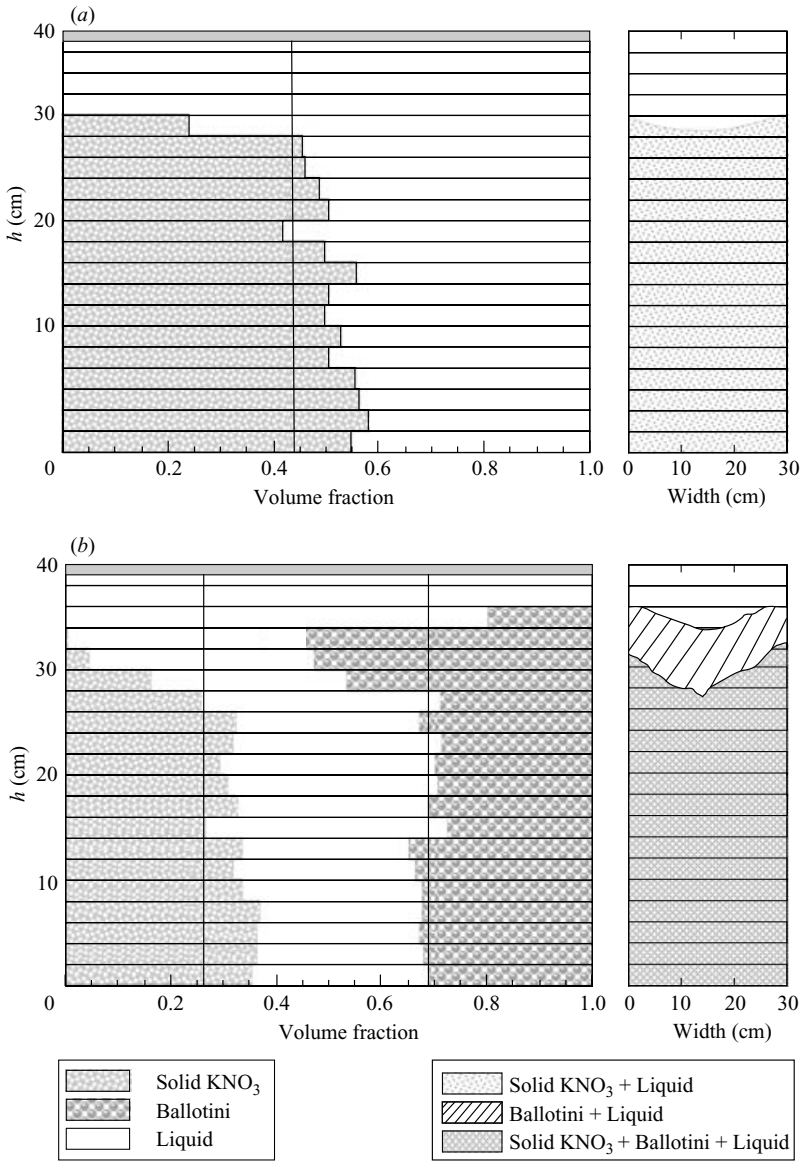


FIGURE 8. The final volume fractions of solid and liquid phases as a function of height, determined from analyses of the residual porous matrices from (*a*) Expt 2a, initially having a solid matrix composed of pure KNO_3 with $\phi_o = 0.437$, and (*b*) Expt 3a, initially having a solid matrix composed of a mixture of glass ballotini and KNO_3, with $\phi_g = 0.306$ and $\phi_s = 0.264$.

2.3.3. *Solid KNO_3 and ballotini in saturated KNO_3 solution*

In four experiments (Expts 3a–c and 4), glass ballotini were introduced as an inert solid phase in the matrix as depicted in figure 3(*c*). This caused a reduction of the volumetric proportion of solid KNO_3 crystals, while still maintaining a uniform initial distribution in a loosely packed granular pile occupying the whole tank. The experimental observations from these experiments were fundamentally similar to those already described in the previous section, except that the interface marking the

https://doi.org/10.1017/S0022112005004830 Published online by Cambridge University Press

complete dissolution of all original solid KNO_3 crystals was in these cases separated from the overlying clear liquid region by a compacted layer of residual ballotini. Since these experiments involved less solid KNO_3 per unit volume in the original solid matrix, the descent rate of the interface marking its disappearance becomes notably more rapid, as shown in figure 6. Representative temperature measurements as functions of time and height for a representative experiment (3c) are presented in figure 9, and measurements of the final volumetric proportions of individual phases determined from analysis of the residual matrix are shown in figure 8(*b*).

3. Theory

We present here a quantitative description of these experimental results with a view both to test our interpretation of the physical fluid dynamics and phase change processes, and to apply the relationships derived to larger-scale natural situations. Owing to the presence of compositional plumes, the experiments evolve in time with an essentially three-dimensional geometry. To describe this in detail would require a large, complicated numerical model. This is to be considered in a following paper (Butler, Huppert & Worster 2005). The approach taken here is to develop a model which is dependent only on time and the one spatial dimension of height. It thus omits the details of the plumes, which could be included by incorporating standard plume theory, as outlined for example by Turner (1979) and Phillips (1991). It does supply, however, a valuable and predictive one-dimensional spatial model which yields the governing parameters of the system in addition to horizontal-averaged values of the flow variables and the interface height. As we see below, in comparing the theoretical results with experimental data, the model is very effective.

3.1. *Solid crystals in saturated solution*

We consider a one-dimensional layer, of height H, comprised initially of a homogeneous mixture of solid crystals, of volume fraction ϕ_0, and saturated interstitial liquid of mass concentration C_0, all at temperature T_0 as exemplified by Expts 2. (The added influence of non-reactive glass ballotini will be considered in § 3.2.) At time $t = 0$ the top of the layer is suddenly brought to temperature T_W ($> T_0$) and maintained thereafter at that temperature. We assume that the heat flux, denoted by Q, is used entirely to dissolve crystals at the top of the layer, which increases the concentration and density of the saturated interstitial liquid. The compositional Rayleigh number in the experiments is much larger than critical, and therefore the dense interstitial liquid drives compositional convection in the porous layer below and, to leading order, mixes the liquid within the pore space so that it becomes spatially uniform. Guided by our experimental observations, we assume that the convective circulation provides an efficient mechanism of recharging the interface with liquid from the lower layer, thereby maintaining a relatively sharp interface with pure liquid above it, and negligible dissolution below it. Furthermore, we assume that there is negligible change in temperature across the dissolving interface, and therefore negligible convective heat flux associated with the compositional convection in the lower layer. The increased concentration of the liquid in the porous layer leads to re-precipitation with an associated increase in the solid fraction, ϕ. The heat released by this crystallization leads to a gradual increase in the temperature of the lower layer, which is assumed to occur at a sufficiently slow rate that the crystals and interstitial liquid remain in a state of thermal and compositional equilibrium. The equilibrium temperature T and concentration C of the liquid in this porous medium is then governed by the liquidus

https://doi.org/10.1017/S0022112005004830 Published online by Cambridge University Press

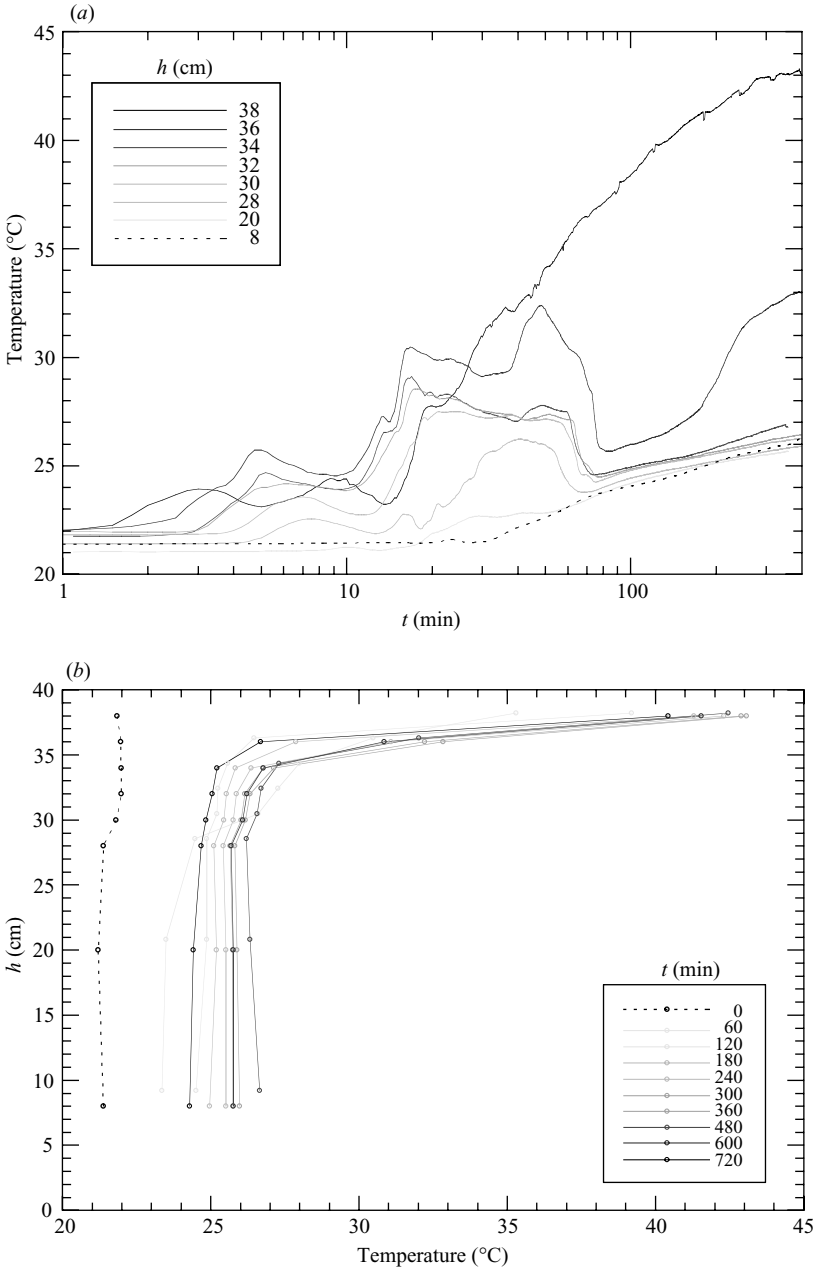


FIGURE 9. The temperature data from an array of eight thermistors at different heights in Expt 3c plotted against (*a*) time, and (*b*) height at selected times.

relationship, which is modelled by the linear approximation

$$C = C_* + mT, \tag{3.1}$$

where C_* and m are constant (figure 1).

The mathematical description of these processes involves the conservation of mass and heat, coupled with the assumption that the heat flux supplied to the top of the

https://doi.org/10.1017/S0022112005004830 Published online by Cambridge University Press

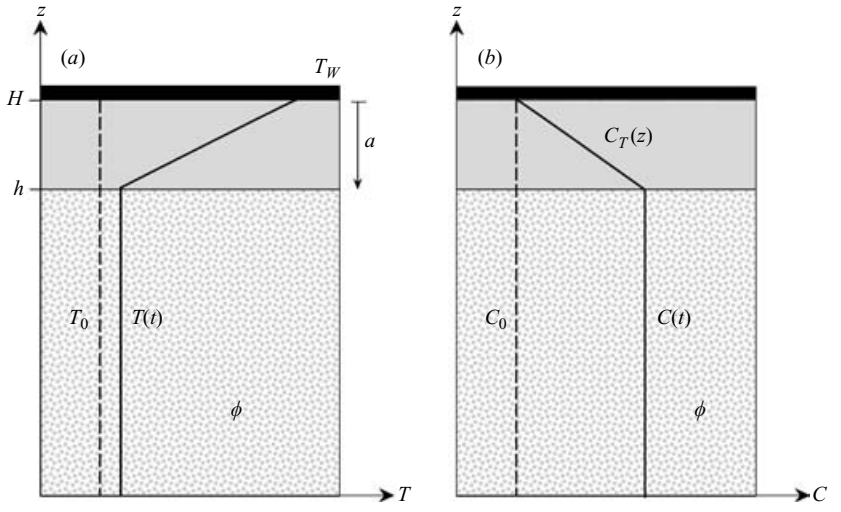


FIGURE 10. A sketch of the vertical profiles of (*a*) temperature and (*b*) concentration.

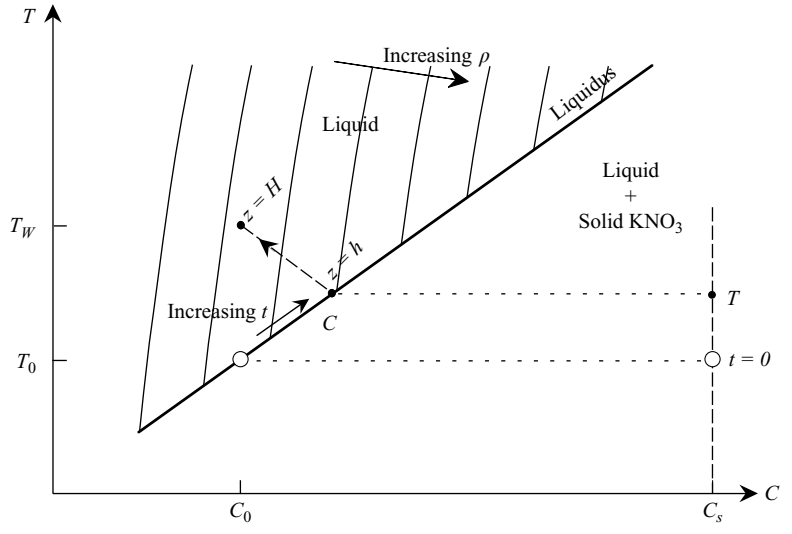


FIGURE 11. A sketch of the evolution on a phase diagram.

crystal pile is used entirely to dissolve the uppermost crystals, while their resultant recrystallization throughout the porous layer below accounts for its thermal evolution. As the interface descends it leaves behind a gravitationally stable concentration profile denoted by $C_T(z)$ with respect to a vertical z-axis, such that

$$C_T[h(t)] = C(t), \tag{3.2}$$

where $h(t)$ is the thickness of the lower porous layer. As indicated by the requirement of the phase diagram (figure 1), $C_T(z)$ is a monotonically decreasing function and so the upper clear layer, in which the temperature increases with height, is stably stratified. A sketch of the vertical profiles is presented in figure 10, and of the evolution on a phase diagram in figure 11, which shows how the temperature and concentration of the interstitial fluid are linked by the liquids; and both increase with time.

https://doi.org/10.1017/S0022112005004830 Published online by Cambridge University Press

Global conservation of solute requires that

$$[\rho_s C_s \phi + \rho_l C(1-\phi)]h + \int_h^H \rho_l C_T(z)\,\mathrm{d}z = M_s', \tag{3.3}$$

where ρ denotes density, with the subscripts s and l indicating values attributable to the solid and liquid respectively, C_s is the solid concentration, which we assume to remain constant and is equal to 1 in our experiments with aqueous solutions, and M_s' is the total mass of solute per unit horizontal area. While ρ_l changes slightly with both temperature and concentration, for simplicity we will make an extended Boussinesq approximation and consider it to remain constant.

Denoting the total amount of solute in the lower layer by Ψ, so that

$$\Psi = [\rho_s C_s \phi + \rho_l C(1-\phi)]\,h, \tag{3.4}$$

we can differentiate (3.3) and use (3.2) to obtain

$$\delta\Psi = \rho_l C \delta h. \tag{3.5}$$

This relationship indicates that as the interface descends, the change of total solute in the lower layer occurs as a result of a flux of solute through the interface which is directly proportional to the concentration in the lower layer and the change in position of the interface. Now substituting $\beta = \rho_s C_s - \rho_l C$ into (3.4) and using (3.5), we obtain, after a little rearrangement,

$$\frac{\delta\beta}{\beta} = \frac{1}{h(1-\phi)}\delta(\phi h). \tag{3.6}$$

Conservation of heat requires that the heat flux supplied to the upper boundary, say Q, is given by

$$Q = -\rho_s \phi L \frac{\mathrm{d}h}{\mathrm{d}t} + \overline{\rho c_p} h \frac{\mathrm{d}T}{\mathrm{d}t} - \rho_s L h \frac{\mathrm{d}\phi}{\mathrm{d}t}, \tag{3.7}$$

where L is the latent heat associated with the phase change, $\overline{\rho c_p} = (\rho c_p)_s \phi + (\rho c_p)_l (1-\phi)$, and the three terms on the right-hand side of (3.7) represent respectively: the latent heat required for dissolution at the interface; the increase in specific heat of the crystal pile; and the latent heat released in the crystal pile associated with the solidification which results as a consequence of the compositional convection driven by melting at the interface. No consideration is given in this general theory to heat taken up by the Perspex walls in the experiment, an aspect which will be evaluated when comparing the experimental data to the theoretical predictions.

The assumption that the convection in the lower layer is driven entirely by the compositional difference reflects the fact that the lines of constant density in the liquid region of the phase diagram shown in figure 11 have a much larger gradient than the liquidus. The effects of composition thus overwhelm those of temperature in determining the density difference to which the convection responds. This fact suggests equating separately the left-hand side with the first term on the right-hand side and the last two terms. This procedure leads to the relationships

$$Q = -\rho_s \phi L \frac{\mathrm{d}h}{\mathrm{d}t}, \tag{3.8}$$

which governs the rate of dissolution at the interface, and

$$\overline{\rho c_p} h \frac{\mathrm{d}T}{\mathrm{d}t} = \rho_s L h \frac{\mathrm{d}\phi}{\mathrm{d}t}, \tag{3.9}$$

https://doi.org/10.1017/S0022112005004830 Published online by Cambridge University Press

which describes the conservation of heat in the lower layer. Thus, in the model the heat flux from the upper boundary melts crystals at the top of the porous medium (3.8); and the interior heat is redistributed without further loss or addition (3.9). Equation (3.9) can be integrated using the initial conditions to obtain

$$\phi - \phi_0 = (\overline{\rho c_p}/\rho_s L)(T - T_0). \tag{3.10}$$

It is now convenient to introduce dimensionless variables in order to simplify the algebraic manipulation and to clarify the key physical controls on the system. We define a dimensionless temperature

$$\theta = (T - T_0)/(T_W - T_0), \tag{3.11}$$

which has initial value 0 and always lies between 0 and 1. In terms of θ, it follows from (3.1) that

$$C = C_0(1 + \gamma\theta), \tag{3.12}$$

where

$$\gamma = m(T_W - T_0)/C_0 \tag{3.13}$$

represents the change in concentration associated with heating the interstitial liquid from the initial temperature to that at the boundary compared to the initial concentration of the liquid. It also follows from (3.10) that

$$\phi = \phi_0(1 + \Lambda\theta), \tag{3.14}$$

where

$$\Lambda = \frac{\overline{\rho c_p}}{\rho_s L \phi_0}(T_W - T_0) \tag{3.15}$$

is an inverse Stefan number and represents the ratio of the thermal energy input at the top of the layer to that required to dissolve all the crystals. It will generally take a value below unity. For Expts 2, $\Lambda \approx 0.3$.

Substituting (3.12) and (3.14) into (3.6) and re-arranging, we obtain

$$\left[\frac{[\Gamma(1 - \phi_0) + \Lambda\phi_0] - 2\Gamma\Lambda\phi_0\theta}{\phi_0(1 - \Gamma\theta)(1 + \Lambda\theta)}\right]\delta\theta = -\frac{\delta y}{y} \tag{3.16}$$

with

$$\theta(y = 1) = 0, \tag{3.17}$$

where $y = h/H$ is the dimensionless depth of the lower crystal pile, and

$$\Gamma = \frac{\rho_l C_0 \gamma}{\rho_s C_s - \rho_l C_0} \tag{3.18}$$

represents the ratio, evaluated in density units, of the change in concentration associated with heating the crystal pile from its initial temperature to the temperature at the upper boundary and the initial difference in concentration between solid crystals and interstitial liquid. For small values of Γ, a small amount of dissolution is sufficient to raise the concentration of the interstitial liquid to that corresponding to saturated liquid at the temperature of the upper boundary. For large values of Γ, a relatively large amount of dissolution is required. For Expts 2, $\Gamma \approx 0.1$.

Equations (3.16) and (3.17) can be solved by the method of partial fractions to obtain a relationship between y and θ which depends on the dimensionless parameters Γ, Λ and ϕ_0 and is, because of the flux condition (3.5), independent of M_s'. The

https://doi.org/10.1017/S0022112005004830 Published online by Cambridge University Press

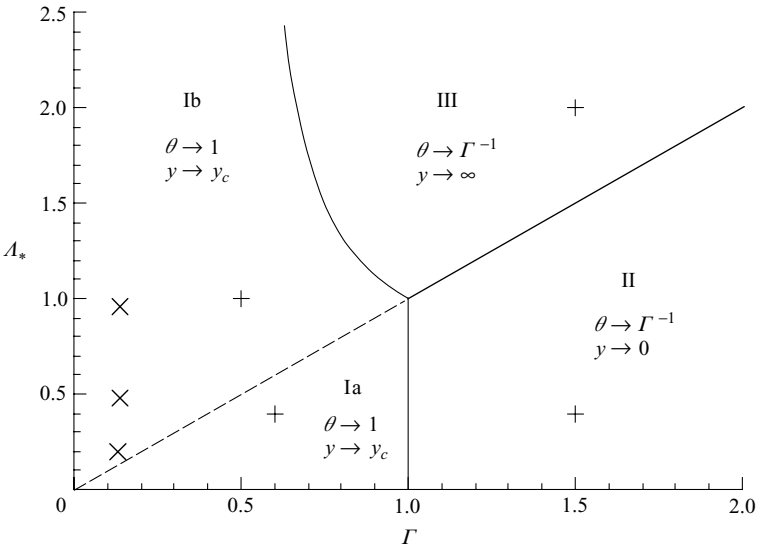


FIGURE 12. The regime diagram for the form of solutions (3.19) and (3.46). For (3.19), the relationship valid without non-reactive particles, $\Lambda_* = \phi_0 \Lambda/(1-\phi_0)$, while for (3.46), which includes the influence of non-reactive particles $\Lambda_* = \phi_0 \tilde{\Lambda}/(1-\phi_0-\chi_0)$. The four + symbols correspond to values used in figure 13. The three × symbols correspond to experimental values.

requisite relationship is

$$y = (1-\Gamma\theta)^{p_1}/(1+\Lambda\theta)^{p_2}, \tag{3.19}$$

where

$$p_1 = \left[(1-\phi_0)\phi_0^{-1} - \Lambda\Gamma^{-1}\right] / \left(1+\Lambda\Gamma^{-1}\right) \quad \text{and} \quad p_2 = 1 + \left[\phi_0(1+\Lambda\Gamma^{-1})\right]^{-1}. \tag{3.20a, b}$$

For the parameter ranges of general relevance here, the relationship (3.19) can take one of the three different forms, appropriate to the regions evaluated in the Appendix and depicted in figure 12. In region I, given by $\Gamma < \min\{1, \Lambda\phi_0[\phi_0(2\Lambda+1)-1]^{-1}\}$, which contains Expts 2, as θ increases from 0 to 1, y decreases from 1 to $y_c \equiv (1-\Gamma)^{p_1}/(1+\Lambda)^{p_2}$. Typical curves are graphed in figure 13. In region II, given by $\Gamma > \max\{1, \phi_0(1-\phi_0)^{-1}\Lambda \equiv \Lambda_*\}$, as y decreases from 1 to 0, θ increases from 0 to Γ^{-1}. A typical curve is graphed in figure 13. In region III, given by $\Lambda > \max\{(1-\phi_0)\phi_0^{-1}\Gamma(2\Gamma-1)^{-1}, (1-\phi_0)\phi_0^{-1}\Gamma\}$, y decreases from 1 to y_c while θ increases from 0 to $\theta_* \equiv (2\Gamma)^{-1} + (1-\phi_0)(2\Lambda\phi_0)^{-1}$, and then, unphysically, increases to infinity as θ increases to Γ^{-1}, as marked in figure 13.

The unphysical result that y can increase with increasing θ is due to the fact that we have not yet taken into account that as ϕ increases to 1 (a totally solid lower layer), the compositional convection can no longer be maintained and the model needs to be changed. The convection will cease somewhat before $\phi = 1$, but for simplicity, and to bring out the fundamental principles, we take $\phi = 1$ as the criterion of change over. From (3.14), $\phi = 1$ when

$$\theta = (1-\phi_0)/(\phi_0\Lambda) = \Lambda_*^{-1} \equiv \theta_1. \tag{3.21a, b, c}$$

There are thus three possible endpoints for θ from the model as stated: (*a*) $\theta = \Gamma^{-1}$, for which $y = 0$ and the whole system eventually becomes liquid; (*b*) $\theta = 1$, for which

https://doi.org/10.1017/S0022112005004830 Published online by Cambridge University Press

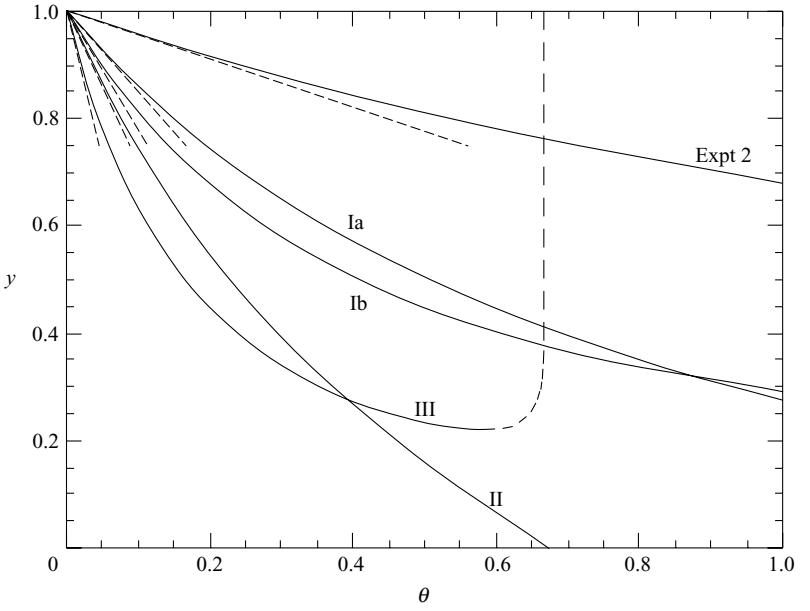


FIGURE 13. Graphs of $y(\theta)$ for $\phi_0 = 0.4$ and $(\Gamma, \Lambda) = (0.6, 0.6)$, Ia; (0.5, 1.5), Ib; (1.5, 0.6), II; (1.5, 3.0), III; and (0.13, 0.3), Expts 2. The dashed straight lines represent the approximation (3.22).

$y = y_c$ and the system evolves to a uniform temperature T_W with a liquid upper layer and a partially solid lower layer; or (*c*) $\theta = \theta_1$, and the system clogs up in finite time.

The conditions under which each of (*a*), (*b*) or (*c*) is selected is determined by the relative values of Γ^{-1}, θ_1 and 1. Since θ is constrained to be less than or equal to 1, for $\Gamma < 1$ either $\Lambda_* > 1$, in which case $\theta_1 < 1$ and (*c*) describes the final state of the model, or $\Lambda_* < 1$, in which case (*b*) describes the final state. For $\Gamma > 1$ either $\Lambda_* > \Gamma$, in which case the final state is again (*c*), or $\Lambda_* < \Gamma$, in which case the final state is (*a*). These three possibilities are depicted in figure 14.

Beyond this final state of the model, in case (*a*), if the temperature T_W at the boundary continues to be maintained, the liquid layer gradually warms up to the uniform temperature T_W by conduction. Case (*b*) already describes the final (uniform temperature) situation. In case (*c*) either both the liquid and solid warm up to the uniform temperature by conduction, or, if T_W exceeds the melting temperature of the pure solid, it melts to lead to a liquid layer at uniform temperature T_W.

If either θ or both Λ and Γ are small, it follows from direct expansion of (3.19) that

$$y = 1 - \left[\Lambda + \Gamma(1-\phi_0)\phi_0^{-1}\right]\theta + O(\Lambda^2\theta^2, \Gamma^2\theta^2), \tag{3.22}$$

that is, to first order in the smallness of either θ or Γ and Λ, y is linear in θ. This approximation is compared with the full solutions in figure 13, from where it is seen that there is excellent agreement between the exact solution and the linear approximation for at least $0.75 \leqslant y \leqslant 1$.

We now complete the calculations by examining the temporal evolution due to the input heat flux, Q. We make the simplifying assumption that the interface descends sufficiently slowly that the stable upper fluid layer remains in conductive equilibrium. Formally, this assumption requires that $\dot{h} \ll \kappa_l/(H-h)$, which is associated with a large

https://doi.org/10.1017/S0022112005004830 Published online by Cambridge University Press

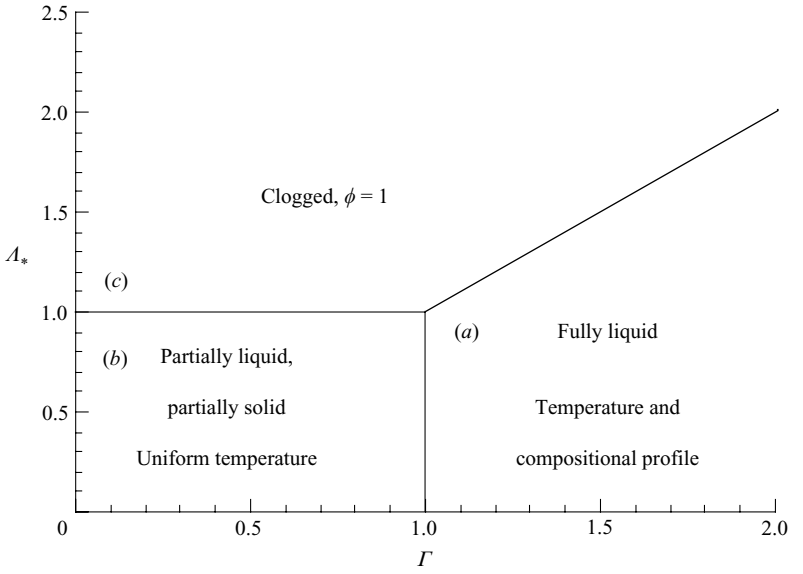


FIGURE 14. The final state of the model (cf. figure 12) allowing for the lower porous medium to become totally solid.

value of the Stefan number (small Λ), as possibly first shown in Turner, Huppert & Sparks (1986) and used to good effect frequently thereafter. With this assumption, the detailed solution of the parabolic heat conduction equation is not needed to determine the flux supplied to the dissolving interface, which is given simply by the relationship

$$Q = (\rho c_p \kappa)_l (T_W - T)/(H - h). \tag{3.23}$$

Inserting this into (3.8) and using (3.11) and (3.14), we obtain

$$\frac{\mathrm{d}y}{\mathrm{d}\tau} = -\frac{(1-\theta)}{(1-y)(1+\Lambda\theta)}. \tag{3.24}$$

$$y(\tau = 0) = 1, \tag{3.25}$$

where the dimensionless time is defined for convenience by $\tau = (\rho c_p \kappa)_l \Lambda t/(\overline{\rho c_p} H^2)$. The solution to (3.24) and (3.25) can be expressed as

$$\tau(y) = \int_y^1 \frac{(1-y)(1+\Lambda\theta)}{1-\theta}\,\mathrm{d}y, \tag{3.26}$$

where θ is given by the inverse of (3.19). For $\theta \ll 1$, which corresponds to $\tau \ll 1$, the terms in θ in (3.26) can be neglected, and thus

$$\tau = \tfrac{1}{2}(1-y)^2[1 + O(\theta)], \tag{3.27a}$$

or

$$1 - y = (2\tau)^{1/2} + O(\tau). \tag{3.27b}$$

It then follows using (3.22) that

$$\theta = \left[\Lambda + \Gamma(1-\phi_0)\phi_0^{-1}\right]^{-1} (2\tau)^{1/2} + O(\tau). \tag{3.27c}$$

Numerical solutions of (3.26) for representative parameters in regions I, II and III are displayed in figure 15 along with the approximations (3.27). It is seen that the

https://doi.org/10.1017/S0022112005004830 Published online by Cambridge University Press

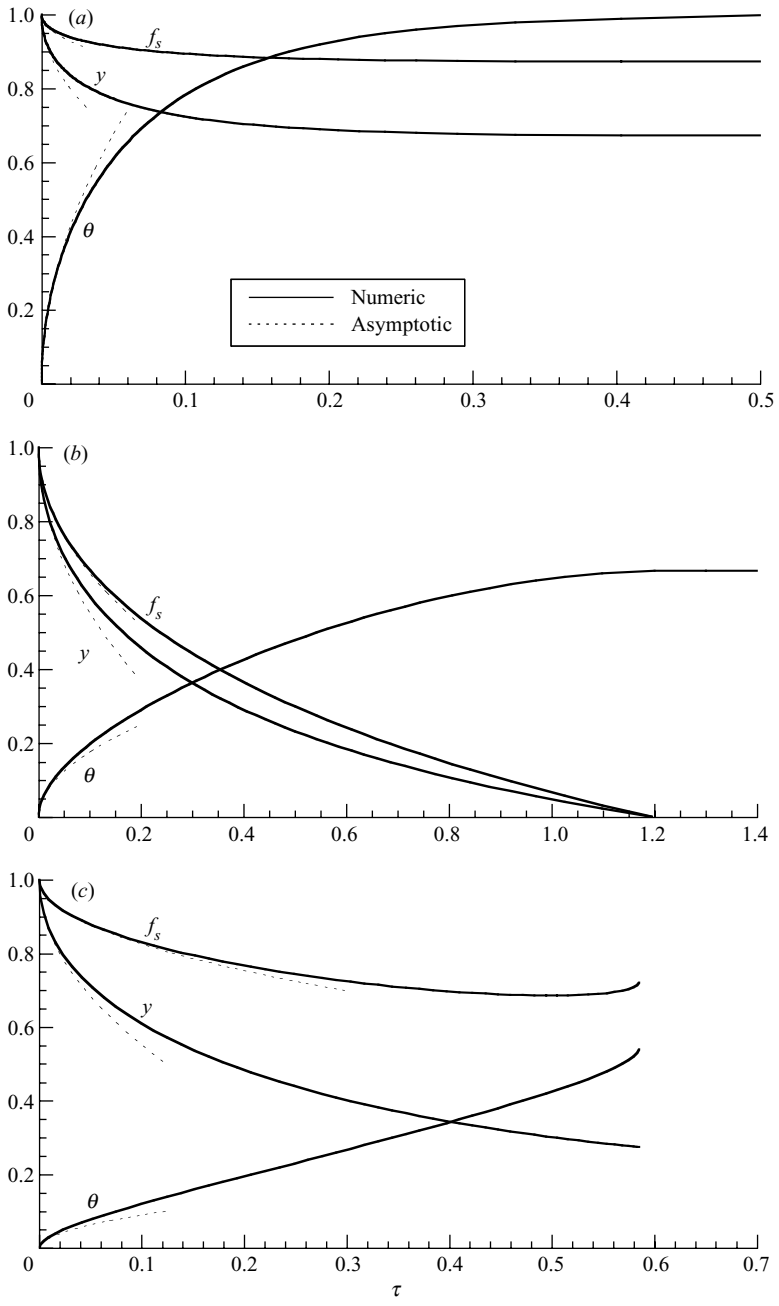


FIGURE 15. Graphs of $\theta(\tau)$, $y(\tau)$ and $f_s(\tau)$ for $\phi_0 = 0.44$ and (*a*) $(\Gamma, \Lambda) = (0.13, 0.3)$; (*b*) $(\Gamma, \Lambda) = (1.5, 0.6)$; and (*c*) $(\Gamma, \Lambda) = (1.5, 3.0)$.

approximations agree well with the numerical solutions (and act as an independent check on them) for sufficiently small values of τ. For region I, as typified by the curves that make up figure 15(*a*), $\theta \to 1$ and $y \to y_c$ as $\tau \to \infty$. For region II (figure 15*b*), $\theta = \theta_*$, $h = 0$ for $\tau > \tau_* \equiv \int_0^1 (1 - y)(1 + \Lambda\theta)(1 - \theta)^{-1}\,\mathrm{d}y$. For region III (figure 15*c*),

https://doi.org/10.1017/S0022112005004830 Published online by Cambridge University Press

$\mathrm{d}\theta/\mathrm{d}\tau \to \infty$ as τ approaches a finite value, say τ_{III}, while θ and h are undefined for $\tau > \tau_{III}$.

The total mass of solid per unit horizontal area, $\mathscr{M}$, in the lower layer at any time is given by $\mathscr{M} = \rho_s \phi h$. Non-dimensionalizing $\mathscr{M}$ by its initial value $\mathscr{M}_0 = \rho_s \phi_0 H$ to determine the fractional mass of solid, f_s, and using (3.14), we may write

$$f_s = (1 + \Lambda\theta)y = 1 - \left[\frac{\Gamma(1-\phi_o)}{\Lambda\phi_0 + \Gamma(1-\phi_o)}\right](2\tau)^{1/2} + O(\tau), \tag{3.28a, b}$$

which is also graphed on figure 15.

These theoretical results can now be compared to the experimental data. But first, the heat taken up by the Perspex sidewalls of the tank must be included in the calculation. Conservation of heat in the lower layer, to replace (3.9), then becomes

$$(\rho c_p)_{eff}\frac{\mathrm{d}T}{\mathrm{d}t} = \rho_s L\frac{\mathrm{d}\phi}{\mathrm{d}t}, \tag{3.29}$$

where the effective heat capacity $(\rho c_p)_{eff}$ is given by

$$(\rho c_p)_{eff} = [W\overline{\rho c_p} + d(\rho c_p)_P]/W \tag{3.30a}$$

$$= \overline{\rho c_p} + 1.1(\rho c_p)_P \tag{3.30b}$$

in terms of the half-width of the layer W, the thickness of the Perspex walls d and the heat capacity of the Perspex $(\rho c_p)_P$ as in table 2. The only change to the calculation already presented is the introduction of an effective value of Λ, Λ_{eff}, defined by

$$\Lambda_{eff} = \frac{(\rho c_p)_{eff}}{\rho_s L\phi_0}(T_W - T_0) \tag{3.31}$$

(cf. (3.15)). (The heat flux Q delivered to the descending interface is unchanged, as is the timescale, which is determined by the dissolution.) For Expts 2, $\Gamma \approx 0.13$, $\Lambda \approx 0.3$ and $\phi_0 \approx 0.44$. Figure 15(a) graphs y, θ and f_s as functions of τ for these values. Figure 16 presents these curves in dimensional form over the timescale of the experiments for $\Lambda_{eff} = 0.46$ and includes the experimental data. The agreement between the two is seen to be very good. From (3.27b), $a \approx H(2t/t_s)^{1/2}$ where the timescale $t_s = \overline{\rho c_p}H^2/[(\rho c_p \kappa)_l \Lambda] = 57\,300$ min, that is, with t in minutes $a = 0.23t^{1/2}$, where the theoretical premultiplicative constant of 0.23 agrees well with the experimental value of 0.22 presented in table 3.

3.2. *Solid crystals plus non-reactive solid in saturated solution*

The analysis proceeds in a way that is similar to that in § 3.1. A layer, of height H, is comprised initially of a homogeneous mixture of solid crystals, of volume fraction ϕ_0, saturated interstitial liquid of mass concentration C_0, and a non-reactive solid, of volume fraction χ_0, all at temperature T_0. At time $t = 0$ the top of the layer is suddenly brought to temperature T_W ($> T_0$) and maintained thereafter at that temperature. As depicted in figure 3(c), this results in the formation of a layer of thickness a of clear fluid of concentration $C_T(z)$, beneath which there is a layer that extends to a depth b below the top and is made up of clear fluid of concentration $C_T(z)$ and non-reactive solid of volume fraction χ_1, the (given) close packing fraction of the solid. Below this lies a layer of thickness $h(t) = H - b$ of solid crystals with volume fraction ϕ, saturated liquid of concentration $C(t)$ and non-reactive solid of volume fraction χ_0. The function $C_T(z)$ is a continuous function of z in the upper two layers and merges

https://doi.org/10.1017/S0022112005004830 Published online by Cambridge University Press

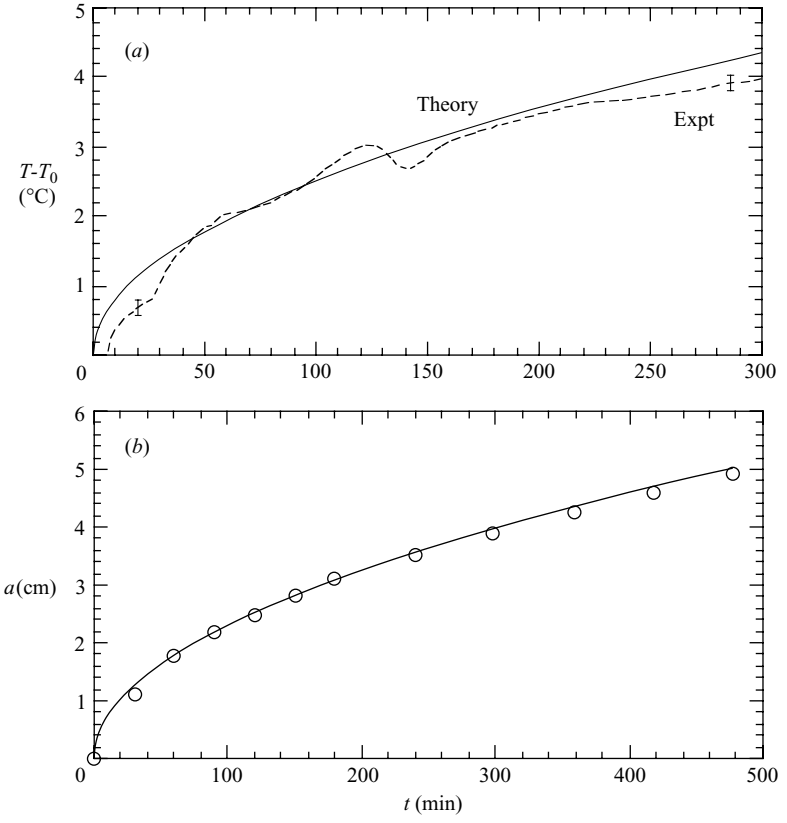


FIGURE 16. Graphs of (*a*) $T-T_0$ and (*b*) a as functions of time for parameter values relevant to Expt 2b, determined numerically (solid curves) and experimentally (dashed curve and circles). The displayed experimental temperature is the mean of readings taken within the porous medium. The error bars correspond to $\pm 0.1\,^{\circ}$C.

	$at^{-1/2}$ (cm min$^{-1/2}$)		$bt^{-1/2}$ (cm min$^{-1/2}$)	
Expt	expt	theory	expt	theory
2b	0.22	0.23	–	–
3c	0.14	0.14	0.26	0.28
4	0.10	0.10	0.37	0.43

TABLE 3. Comparisons between the experimentally determined values of $at^{-1/2}$ and $bt^{-1/2}$, both in cm min$^{-1/2}$, with the theoretical predictions.

continuously with $C(t)$ in the lowest layer, so that, as in (3.2),

$$C_T[h(t)] = C(t). \tag{3.32}$$

A sketch of the temperature, concentration and non-reactive solid fraction is presented in figure 17.

Conservation of non-reactive solid can be written as

$$(b-a)\chi_1 = b\chi_0 \tag{3.33}$$

https://doi.org/10.1017/S0022112005004830 Published online by Cambridge University Press

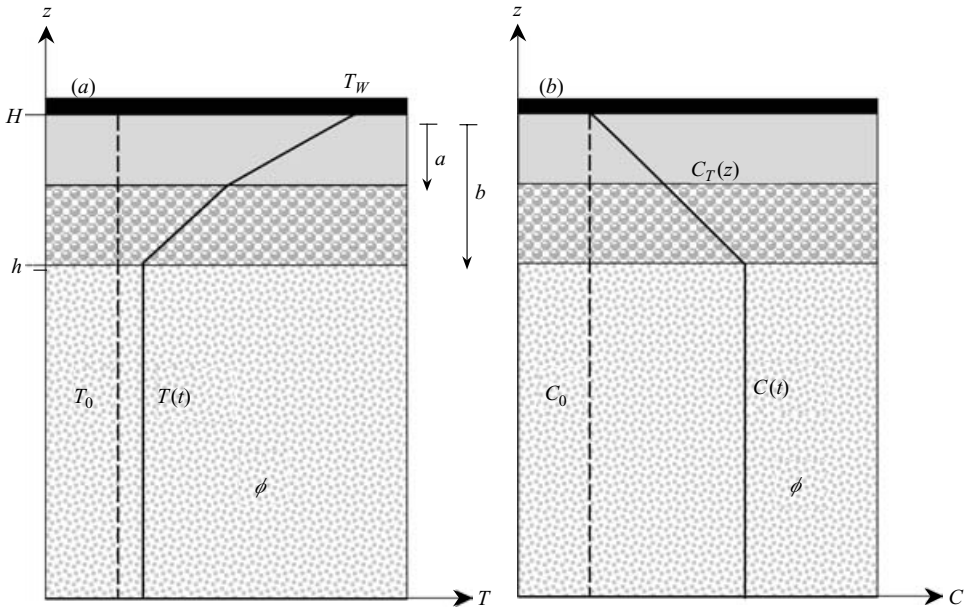


FIGURE 17. A sketch of the vertical profiles of (*a*) temperature and (*b*) concentration for the situation when non-reactive particles are included.

from which it follows that the thickness of the uppermost layer is linearly related to that of the middle layer by

$$a = (\chi_1 - \chi_0)b/\chi_1 \tag{3.34}$$

where χ_{10} is a constant. Global conservation of solute requires that

$$[\rho_s C_s \phi + \rho_l C(1-\phi-\chi_0)]h + \int_h^{h_+} \rho_l(1-\chi_1)C_T(z)\,\mathrm{d}z + \int_{h_+}^{H} \rho_l C_T(z)\,\mathrm{d}z = M_s', \tag{3.35}$$

where $h_+ = h + b - a$ is the combined thickness of the lowest and middle layers. Denoting the total amount of solute in the lowermost layer by Ψ_b, so that

$$\Psi_b = [\rho_s C_s \phi + \rho_l C(1-\phi-\chi_0)]\,h, \tag{3.36}$$

we can differentiate (3.35) and use (3.32) to obtain

$$\delta\Psi_b = \rho_l \chi_1 C_T\,[h_+(t)]\,\delta h_+ + \rho_l(1-\chi_1)C(t)\delta h. \tag{3.37}$$

While formally correct, (3.37) is difficult to handle because of the appearance on the right-hand side of the unknown $C_T[h_+(t)]$. However, since the right-hand side represents the total flux of solute through the lower interface, we can express (3.37) in analogy with (3.5) as

$$\delta\Psi_b = \rho_l(1-\chi_1)C\delta h, \tag{3.38}$$

which circumvents the appearance of $C_T[h_+(t)]$. Introducing $\beta = \rho_s C_s - \rho_l C$ into (3.36) and using (3.38), we obtain

$$h(\phi + \chi_0 - 1)\delta\beta + \beta\delta(\phi h) - \rho_l(\chi_1 - \chi_0)C\delta h = 0 \tag{3.39}$$

as the counterpart of (3.6).

https://doi.org/10.1017/S0022112005004830 Published online by Cambridge University Press

Conservation of heat in the lower layer requires

$$\widetilde{\rho c_p} h \frac{\mathrm{d}T}{\mathrm{d}t} = \rho_s L h \frac{\mathrm{d}\phi}{\mathrm{d}t}, \tag{3.40}$$

where the average denoted by a tilde is defined by

$$\widetilde{\rho c_p} = (\rho c_p)_s \phi + (\rho c_p)_b \chi + (\rho c_p)_l (1 - \phi - \chi) \tag{3.41}$$

and the subscript b indicates a value attributable to the non-reactive solid (modelled by ballotini in the experiments). Integrating (3.40) with the appropriate initial conditions and introducing the non-dimensional θ defined by (3.11), we find that

$$\phi = \phi_0 (1 + \tilde{\Lambda}\theta), \tag{3.42}$$

in terms of the augmented inverse Stefan number

$$\tilde{\Lambda} = \frac{\widetilde{\rho c_p}}{\rho_s L \phi_0} (T_W - T_0), \tag{3.43}$$

which for Expts 3 is approximately 0.5 and for Expt 4 approximately 1. These values are larger than those for Expts 2 due to the lower volume fraction of crystals which take part in the dissolution process.

Substituting (3.12), (3.42) and (3.43) into (3.39), and re-arranging the result, we obtain

$$\left[\frac{[\Gamma(1 - \phi_0 - \chi_0) + \tilde{\Lambda}\phi_0] - 2\Gamma\tilde{\Lambda}\phi_0\theta}{\phi_0(1 - \Gamma\theta)(1 + \tilde{\Lambda}\theta) + \Delta(1 + \gamma\theta)} \right] \delta\theta = -\frac{\delta y}{y}, \tag{3.44}$$

where

$$\Delta = \frac{\rho_l(\chi_1 - \chi_0)C_0}{\rho_s C_s - \rho_l C_0} \tag{3.45}$$

and represents the ratio, evaluated in density units, of the initial concentration of the interstitial liquid and the initial difference in concentration between solid crystals and interstitial liquid times the difference in volume fraction of the non-reactive solid due to compaction.

The analytic solution of (3.44) subject to (3.17) is cumbersome, and the solution is best determined numerically. However, for our experiments $\Delta \approx 0.04$ (Expts 3) and 0.02 (Expt 4) and the influence of the term proportional to Δ is small. In the limit $\Delta \equiv 0$, equation (3.44) is then identical in form to (3.16) and therefore its solution and interpretations can be taken over directly from § 3.1. The solution can thus be written as

$$y = (1 - \Gamma\theta)^{p_3} / (1 + \tilde{\Lambda}\theta)^{p_4}, \tag{3.46}$$

where

$$p_3 = \left[(1 - \phi_0 - \chi_0)\phi_0^{-1} - \tilde{\Lambda}\Gamma^{-1}\right] / \left(1 + \tilde{\Lambda}\Gamma^{-1}\right) \quad \text{and}$$
$$p_4 = 1 + (1 - \chi_0)[\phi_0(1 + \tilde{\Lambda}\Gamma^{-1})]^{-1}. \tag{3.47a, b}$$

The similarities between (3.20) and (3.47) indicate that the solutions of (3.47) take different forms in the different regions of figure 12 as long as the vertical axis is interpreted as $\phi_0\tilde{\Lambda}/(1 - \phi_0 - \chi_0)$.

If either θ or both $\tilde{\Lambda}$ and Γ are small, integration of (3.44) subject to (3.17) indicates that

$$y = 1 - [\tilde{\Lambda}\phi_0 + \Gamma(1 - \phi_0 - \chi_0)](\phi_0 + \Delta)^{-1}\theta + O(\tilde{\Lambda}^2\theta^2, \Gamma^2\theta^2). \tag{3.48}$$

https://doi.org/10.1017/S0022112005004830 Published online by Cambridge University Press

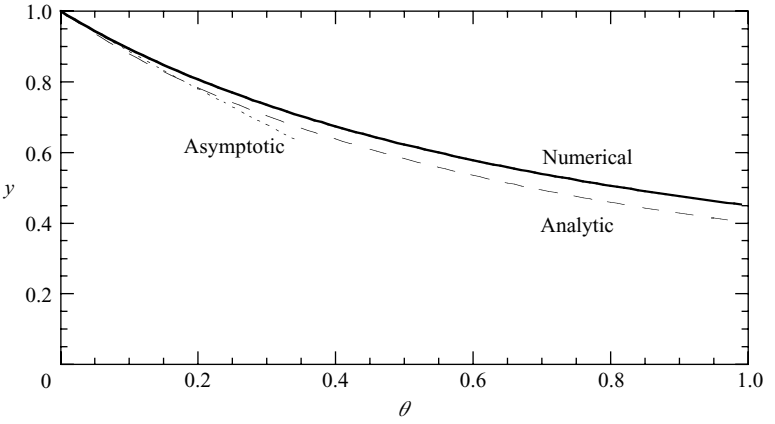


FIGURE 18. The numerically determined $y(\theta)$ compared to its analytic ($\Delta \equiv 0$) and asymptotic ($\theta \to 0$) approximations for $\Gamma = 0.142$, $\tilde{\Lambda} = 0.957$, $\phi_0 = 0.148$, $\chi_0 = 0.450$ and $\chi_1 = 0.582$.

Figure 18 presents curves of the numerically determined $y(\theta)$ which satisfies (3.44) subject to (3.17), along with the asymptotic relationship (3.48) and the analytic approximations (3.46), obtained by setting $\Delta = 0$, for parameter values approximate to Expt 4. These are $\Gamma = 0.142$, $\tilde{\Lambda} = 0.957$, $\phi_0 = 0.148$, $\chi_0 = 0.450$ and $\chi_1 = 0.582$. The agreement between the numerical solution and the two approximations is good.

By conservation of heat, the heat flux from the top of the container Q is given by each of the relationships

$$Q = -\rho_s \phi L \frac{\mathrm{d}h}{\mathrm{d}t} \tag{3.49}$$

$$= (\rho c_p \kappa)_l (T_W - T_I)/a \tag{3.50}$$

$$= (\widehat{\rho c_p \kappa})(T_I - T)/(b - a), \tag{3.51}$$

where $T_I(t)$ is the temperature at the interface between the middle and uppermost layers (see figure 17) and a caret represents the average appropriate to the middle layer, i.e. $(\widehat{\rho c_p \kappa}) = (\rho c_p \kappa)_b \chi_1 + (\rho c_p \kappa)_l (1 - \chi_1)$. Equation (3.49) links Q to the rate of dissolution; (3.50) links it to the heat flux through the uppermost layer; and (3.51) to that in the middle layer, using the approximate solution of the conduction equation, as discussed in the paragraph preceeding (3.23).

Equating (3.50) to (3.51) and using (3.34), we can write

$$T_I = [(\rho c_p \kappa)_l T_W + \widehat{\rho c_p \kappa} \chi_{10} T]/[(\rho c_p \kappa)_l + \widehat{\rho c_p \kappa} \chi_{10}] \tag{3.52}$$

which, when inserted into either (3.50) or (3.51) indicates that

$$Q = \frac{(\rho c_p \kappa)_l \widehat{\rho c_p \kappa}}{[(\rho c_p \kappa)_l + \widehat{\rho c_p \kappa} \chi_{10}]} \frac{\chi_1}{\chi_0} \frac{T_W - T}{H - h}, \tag{3.53}$$

where $\chi_{10} = (\chi_1 - \chi_0)/\chi_0$.

Substituting (3.53) into the left-hand side of (3.49), using (3.11) and the non-dimensionalization of $y = h/H$, we obtain

$$\frac{\mathrm{d}y}{\mathrm{d}\eta} = \frac{-(1 - \theta)}{(1 - y)(1 + \tilde{\Lambda}\theta)}, \tag{3.54}$$

https://doi.org/10.1017/S0022112005004830 Published online by Cambridge University Press

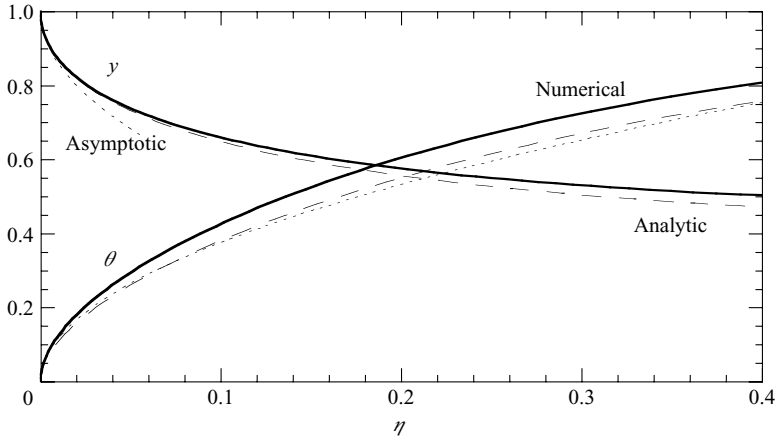


FIGURE 19. The numerically determined $y(\eta)$ and $\theta(\eta)$ compared to their analytic ($\Delta \equiv 0$) and asymptotic ($\eta \to 0$) approximations for the same parameter values as in figure 18.

which is to be solved in conjunction with

$$y(\eta = 0) = 1, \tag{3.55}$$

where the dimensionless time $\eta = t/t_B$ with the timescale

$$t_B = \frac{[(\rho c_p \kappa)_l + \widehat{\rho c_p \kappa}\,\chi_{10}]}{(\rho c_p \kappa)_l \widehat{\rho c_p \kappa}} \frac{\chi_0}{\chi_1} \frac{\rho_s \phi_0 L H^2}{T_W - T_0}. \tag{3.56}$$

Using the same arguments as in § 3.1, we can write the solution of (3.54) and (3.55) for small η as

$$1 - y = (2\eta)^{1/2} + O(\eta) \tag{3.57}$$

and thus, using (3.48),

$$\theta = (\phi_0 + \Delta)[\tilde{\Lambda}\phi_0 + \Gamma(1 - \phi_0 - \chi_0)]^{-1}(2\eta)^{1/2} + O(\eta). \tag{3.58}$$

Figure 19 presents, for the parameter values of Expt 4, graphs of $y(\eta)$ and $\theta(\eta)$ along with the asymptotic relationships (3.57) and (3.58) and the curves obtained by integrating (3.54) and (3.55) using the analytic relationship (3.46).

For Expt 3c, $\Gamma = 0.135$, $\tilde{\Lambda} = 0.481$, $\phi_0 = 0.275$, $\chi_0 = 0.293$ and $\chi_1 = 0.582$. Thus $t_B = 30\,000$ min, while for Expt 4, using the parameter values listed above, $t_B = 14\,200$ min. Using these parameters, (3.34) and the asymptotic relarionship (3.57), we can calculate the theoretically predicted values for $at^{-1/2}$ and $bt^{-1/2}$ compiled in table 3. The agreement between these values and the experimentally determined values is seen to be very good, except for the somewhat higher theoretical value for $bt^{-1/2}$ of Expt 4. Looking back over our experimental notes, we ascribe this difference to an inadvertantly somewhat loose packing of the crystals near the top of this experiment. figure 20 plots the experimentally determined mean temperature of the lower layer and the heights of the two interfaces for Expt 3c as functions of time and compares these to the theoetically predicted results.

4. Summary and discussion

This study was aimed at investigating what happens when a homogeneous porous medium consisting of crystals, saturated liquid and non-reactive particles is heated

https://doi.org/10.1017/S0022112005004830 Published online by Cambridge University Press

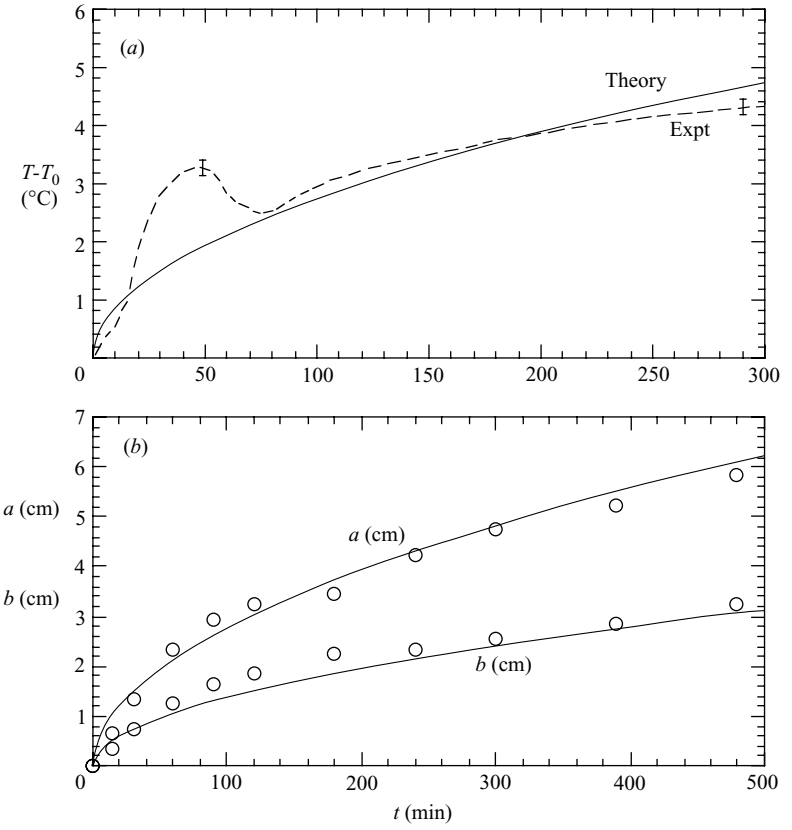


FIGURE 20. Graphs of (*a*) $T - T_0$ and (*b*) a and b as functions of time for parameter values relevant to Expt 3c, determined numerically (solid curves) and experimentally (dashed curve and circles). The displayed experimental temperature is the mean of readings taken within the lowest layer. The error bars correspond to $\pm 0.1\,^{\circ}\mathrm{C}$.

uniformly from above. Laboratory experiments were conducted with a matrix of KNO_3 crystals and non-reactive glass ballotini, bathed in saturated aqueous KNO_3. The initially homogeneous medium evolved into a stratified three-layer system. The uppermost layer consisted of clear aqueous KNO_3; the middle layer consisted of closely packed ballotini bathed in aqueous KNO_3; and the lower layer was made up of a porous medium of KNO_3 crystals, ballotini and saturated aqueous KNO_3, in which the volume fraction of KNO_3 crystals had increased compared to its initial value at the expense of the aqueous phase. This three-layer system was the result of the heat flux supplied at the top of the system being transported freely through the two upper layers and dissolving KNO_3 crystals at the upper boundary of the lower layer. The resulting heavy melt drives compositional convection, which redistributes enriched aqueous KNO_3 uniformly throughout the lower layer, where it recrystallizes to restore chemical equilibrium. The crystallization and associated release of latent heat leads to a gradual increase in both the temperature and solid fraction of the lower layer.

We built a one-dimensional mathematical model to describe the evolution of the system averaged in the horizontal plane. The model was based on the following assumptions. The entire heat flux from the top of the system was used to dissolve the crystals at the interface between the lowermost and middle layers; the interstitial

https://doi.org/10.1017/S0022112005004830 Published online by Cambridge University Press

aqueous KNO_3 was in thermodynamic equilibrium with the surrounding crystals; it was well mixed and hence spatially uniform in temperature and concentration; and there was no transport of solute in the upper region due to either diffusion or advection. The results are dependent on two non-dimensional parameters: $\tilde{\Lambda}$, an augmented inverse Stefan number, and Γ, a concentration change due to the dissolution of KNO_3. There was very good agreement between our theoretical predictions and laboratory data on the horizontally averaged interface positions and, after allowance for heat transfer down the sidewalls of the experimental tank, the temperature in the lower layer as functions of time.

One of the results of the mathematical model is the evaluation of a timescale for the evolution of the system. Detailed expressions for this are given in the previous section; here we present an expression in which, for simplicity, we assign identical values to solid and liquid for each of the physical parameters. The time scale, τ_s, is then given by

$$\tau_s = \left[\frac{\phi_0 L}{c_p(T_W - T_0)}\right]\frac{H^2}{\kappa}, \tag{4.1}$$

which is the product of a porous-medium Stefan number and a conductive timescale. For our experiments, of duration of order 10 h, $\tau_s \approx 1000$ h. Thus the experiments capture only the beginnings of the evolution, but the agreement between theoretical results and experimental data over this time lends confidence to the validity of the model for longer times. However, it might be suggested that at later times, when the supply of heat is less, an increasing fraction of this heat may diffuse into the reactive porous layer rather than be used entirely for producing relatively heavy melt, leading to vigorous compositional convection. Nevertheless the agreement between the model and the experiments over the initial period is encouraging.

Fluid interaction with reactive porous media occurs in a variety of geological situations, including, for example, the migration of acidic groundwater through permeable limestones, groundwater circulation through soluble evaporite deposits and the economically important concentration of ore minerals by the scavenging action of hydrothermal systems (Phillips 1991). An immediate application of the present study is an elucidation of the complexities of cumulate layering observed in many plutonic igneous intrusions, such as on Rum (NW Scotland).

Cumulate rocks are considered to form as assemblages of loosely packed crystals settling on the floor of large basaltic magma chambers. They invariably show phase layering, defined by abrupt changes in the modal proportions of their constituent mineral grains. Layered cumulate sequences also frequently display cyclic repetition of phase assemblages, which are interpretted as the successive accumulation of crystals settling from discrete batches of new hot magma emplaced above the cumulate pile following periodic chamber replenishment events (Huppert & Sparks 1980). Our investigations reveal that the juxtaposition of relatively hot primitive magma above an existing porous cumulate pile may result in extensive redistribution of selected mineral phases by compositionally driven convection, and could either generate layering within an initially homogeneous cumulate, or substantially modify a pre-existing layered structure. Our model envisages that the replenished hot magma acts simply as a heat source, and is not involved in any density-driven exchange flow itself. Using geologically appropriate values of the physical parameters in equation (4.1), we estimate that, independent of the details of the phase diagram, the timescale for such effects typically varies from months for a cumulate body of order 1 m deep to decades for one 10 m deep, and is therefore entirely reasonable within the context

https://doi.org/10.1017/S0022112005004830 Published online by Cambridge University Press

of cooling magma intrusions. We plan to expand the geological consequences of this research in a forthcoming paper.

We thank Professor R. S. J. Sparks for helpful comments. The manuscript was completed while one of us (H. E. H.) was a Visiting Gladden Fellow at the University of Western Australia. He is grateful to Professor J. Imberger and all the staff at the Centre for Water Research for the stimulating environment they supplied during his visit. The research was further supported by awards from EU RTN Euromelt, the Isaac Newton Trust and the Royal Society small grants scheme.

Appendix. The various forms of $y(\theta)$

Consider

$$y(\theta) = (1 - \Gamma\theta)^{p_1}/(1 + \Lambda\theta)^{p_2}, \tag{A 1}$$

where

$$p_1 = \left[(1 - \phi_0)\phi_0^{-1} - \Lambda\Gamma^{-1}\right]/(1 + \Lambda\Gamma^{-1}) \quad \text{and} \quad p_2 = 1 + [\phi_0(1 + \Lambda\Gamma^{-1})]^{-1}. \tag{A 2a, b}$$

as derived in § 3.1, under the stipulation that both y and θ lie between 0 and 1 inclusive and each of Γ, Λ and $p_2 \geqslant 0$. From (3.16), (A 1) satisfies

$$\frac{\mathrm{d}y}{\mathrm{d}\theta} = -\frac{2\Gamma\Lambda(\theta_* - \theta)y}{(1 - \Gamma\theta)(1 + \Lambda\theta)} \tag{A 3a}$$

$$= -2\Gamma\Lambda(\theta_* - \theta)(1 - \Gamma\theta)^{p_1 - 1}(1 + \Lambda\theta)^{-p_2 - 1} \tag{A 3b}$$

$$= -2\Gamma\Lambda\theta_* \qquad (\theta = 0), \tag{A 4}$$

where

$$\theta_* = \tfrac{1}{2}[(1 - \phi_0)(\Lambda\phi_0)^{-1} + \Gamma^{-1}] > 0, \tag{A 5a, b}$$

and (A 4) indicates that $y(0)$ has a negative slope at $\theta = 0$. Comparing (A 2a) with (A 5), we find that p_1 and $\theta_* - \Gamma^{-1}$ are both positive or negative together.

For positive p_1, from (A 1), (A 3b) and (A 5), $y(\theta)$ monotonically decreases until $y = 0$ when $\theta = \Gamma^{-1}$, which is less than θ_*, as is sketched in figure 13. This form of $y(\theta)$ for $\Gamma > 1$ makes up region II of figure 12. If $\Gamma < 1$, then θ has increased to unity, the maximum allowable, at $y = y_c \equiv (1 - \Gamma)^{p_1}/(1 + \Lambda)^{p_2}$. This form of $y(\theta)$ makes up region Ia. Both regions Ia and II require p_1 to be positive, i.e. $\Lambda < \Gamma(1 - \phi_0)\phi_0^{-1}$ with the boundary dividing them given by $\Gamma = 1$, as depicted in figure 12.

For negative p_1, as is clear from (A 1), $y(\theta)$ can never be zero. As θ increases from 0, y decreases (as indicated by (A 3b)) until at $\theta = \theta_*$, $\mathrm{d}y/\mathrm{d}\theta = 0$. For $\theta > \theta_*$, $y(\theta)$ increases monotonically to infinity at Γ^{-1}. Because of the increase in y, corresponding to an *ascent* of the interface, this part of the curve is not relevant to the physical situation being considered. The physically appropriate part of the curve ends: either at $\theta = 1$ at $y = y_c$ (if $\theta_* > 1$), which is depicted in figure 13 and makes up region Ib and contains Expts 3; or at $\theta = \theta_*$ (if $\theta_* < 1$), as sketched in figure 13 and makes up region III. Both regions Ia and III require $p_1 < 0$, or $\Lambda > \Gamma(1 - \phi)\phi_0^{-1}$ with their dividing boundary given by $\theta_* = 1$ or $\Lambda = (1 - \phi)\phi_0^{-1}\Gamma/(2\Gamma - 1)$.

REFERENCES

Bear, J. 1979 *Dynamics of Fluids in Porous Media*. Elsevier.

Butler, S. L., Huppert, H. E. & Worster, M. G. 2005 Numerical modelling of convection in a reactive porous medium with a mobile mush-liquid interface. *J. Fluid Mech.* (in preperation).

https://doi.org/10.1017/S0022112005004830 Published online by Cambridge University Press

Carslaw, H. S. & Jaeger, J. C. 1959 *Conduction of Heat in Solids*. Oxford University Press.

Hallworth, M. A. 1998 Laboratory investigations of geological fluid flows. PhD Thesis, Anglia Polytechnic University.

Huppert, H. E. 1990 The fluid mechanics of solidification. *J. Fluid Mech.* **212**, 209–240.

Huppert, H. E. & Sparks, R. S. J. 1980 The fluid dynamics of a basaltic magma chamber replenished by influx of hot, dense ultrabasic magma. *Contrib. Min. Petrol*, **75**, 279–289.

Irvine, T. N. 1982 Terminology for layered intrusions. *J. Petrol.* **23**, 127–162.

Irvine, T. N. 1987 Appendix 2. Processes involved in the formation and development of layered igneous rocks. In *Origins of Igneous Layering*. (ed I. Parsons), pp. 649–656. D. Reidel.

Jupp, T. E. & Woods, A. W. 2003 Thermally driven reaction fronts in porous media. *J. Fluid Mech.*, **484**, 329–346.

Kerr, R. C. & Tait, S. R. 1986 Crystallization and compositional convection in a porous medium cooled from below with application to layered igneous intrusions. *J. Geophys. Res.* **91**, 3591–3608.

Phillips, O. M. 1991 *Flow and Reactions in Permeable Rocks*. Cambridge University Press.

Sparks, R. S. J., Huppert, H. E., Kerr, R. C., McKenzie, D. P. & Tait, S. R. 1985 Postcumulus processes in layered intrusions. *Geol. Mag*, **122**, 555–568.

Turner, J. S. 1979 *Buoyancy Effects in Fluids*. Cambridge University Press.

Turner, J. S., Huppert, H. E. & Sparks, R. S. J. 1986 Komatiites II: Experimental and theoretical investigations of post-emplacement cooling and crystallization. *J. Petrol.* **27**, 397–439.

Wager, L. R. & Brown, G. M. 1968 *Layered Igneous Rocks*. Oliver & Boyd, Edinburgh.

Wager, L. R. & Brown, G. M. & Wadsworth, W. J. 1960 Types of igneous cumulates. *J. Petrol.* **1**, 73–85.

Washburn, E. W. (Ed.) 1962 *International Critical Tables of Numerical data: Physics, Chemistry and Technology*. National Academic Press.

Weast, R. C. (Ed.) 1971 *CRC Handbook of Chemistry and Physics*. The Chemical Rubber Company.

Worster, M. G. 2000 Solidification of fluids. In *Perspectives in Fluid Dynamics* (ed. G. K. Batchelor, H. K. Moffatt & M. G. Worster). Cambridge University Press.

https://doi.org/10.1017/S0022112005004830 Published online by Cambridge University Press